Numerical simulation of electrical transport in rocks under mechanical action

Tiago Romano Ferreira Queiroz
Integrated MSc in Engineering Physics
Physics Department
2014

Supervisor
Teresa Monteiro Seixas, Associate Professor, FCUP

Co-Supervisor
Manuel António Salgueiro da Silva, Associate Professor, FCUP

U.PORTO

FACULDADE DE CIÊNCIAS
UNIVERSIDADE DO PORTO

Todas as correções determinadas pelo júri, e só essas, foram efetuadas.

O Presidente do Júri,

Porto, _____/_____/_____

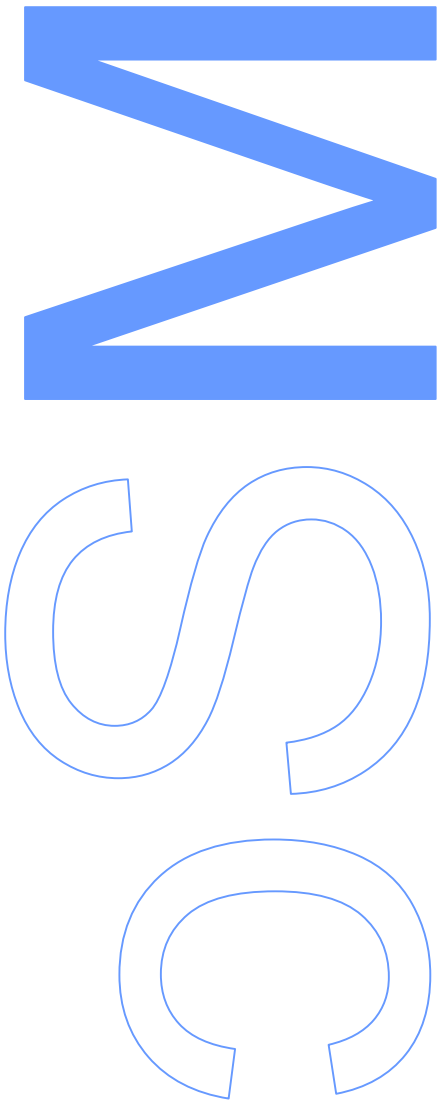

Acknowledgements

First I would like to thank Prof. Teresa Seixas and Prof. Manuel Silva for all the support provided during my dissertation.

I also would like to thank Dr. Hugo Silva along with Prof. Teresa Seixas, for giving me the opportunity of participating in the AEARAM Project.

Thank you Fábio Domingues and Márcio Lima, for providing me the technical support I needed in order to complete the simulations.

I would also like to acknowledge for the support provided by FCT, Project AEARAM.

Finally I would like to thank you Anita for all your patience and support. Without your help, probably I would not be able to complete my dissertation.

Tiago Queiroz

Abstract

In this dissertation we performed a numerical simulation of the electrical behavior of a rock sample under inelastic deformation. For this purpose, we adopted the formalism and methods usually applied to the simulation of semiconductor devices, with appropriate changes to reflect the differences between semiconductor and insulator behavior typical of most rocks. It is assumed that charge generation events occurring inside or on the borders of the deformation region can be modelled as transient charge generation functions. We intend to numerically determine, at any stress-strain state of a sample of a rock, the space charge distribution and the current-voltage characteristic curve. We start by explaining that the electrical behavior of rocks can be described using an adaptation of the formalism applied to semiconductors; then we introduce the equations we intend to use, explaining the differences between the semiconductor equations and the equations that describe the behavior of rocks.

The Gauss-Seidel with over relaxation method was used to solve Poisson's equation, and the Scharfetter-Gummel scheme was adopted in order to discretize the current and continuity equations. Some information about the Scharfetter-Gummel scheme will be provided, and the discretization of all equations will be briefly explained along with its requirements. The code used in the simulation will be fully described, and the analysis of space charge distribution and the current-voltage characteristic curve will take into account five types of functions of carrier generation rate, with stationary potential at the left node, potential varying in time (T = 300 K).

Resumo

Nesta dissertação foi realizada uma simulação numérica do comportamento elétrico de uma amostra de rocha sob deformação inelástica. Para isso, adotou-se o formalismo e os métodos usualmente aplicados para a simulação de dispositivos semicondutores, com alterações que refletem as diferenças entre o comportamento semiconductor e o comportamento isolador típico da maioria das rochas. Supõe-se que os eventos de geração de carga que ocorrem dentro ou na fronteira da região de deformação podem ser modelados como funções transitórias de geração de carga. Pretende-se determinar numericamente, em qualquer estado de tensão-deformação de uma amostra de rocha, a distribuição de carga espacial e a curva característica corrente-tensão. Começamos por explicar que o comportamento elétrico de rochas pode ser descrito usando uma adaptação do formalismo aplicado aos semicondutores; em seguida, apresentamos as equações que pretendemos utilizar, explicando as diferenças entre as equações de semicondutores e as equações que descrevem o comportamento de rochas.

Utilizou-se o método Gauss-Seidel (SOR) na resolução da equação de Poisson, e o esquema Scharfetter-Gummel na discretização das equações da corrente e de continuidade. Algumas informações sobre o esquema de Scharfetter-Gummel serão fornecidas, e a discretização de todas as equações será explicada brevemente, juntamente com as suas exigências. O código usado na simulação será totalmente descrito, e a análise de distribuição de carga espacial e a curva característica de corrente-tensão terá em conta cinco tipos de funções de taxa de geração de transportadores de carga, com o potencial fixo no nodo esquerdo e potencial variável no tempo (T = 300 K).

Table of Contents

List of figures

Chapter 1

Introduction

The Physics of rocks is fundamental for geosciences, especially in areas such as seismology and volcanology.

In seismology, being able to know in advance when and where an earthquake will occur, and with information about its magnitude, is a goal that although there is research for more than 100 years, there is still no conclusive answer for that. Some pre-seismic signals have been studied over the years:

- Dilatancy theory - When rocks are subjected to stress, they expand normal to the stress vector and change their pore volume, which can provoke variations in the resistivity [1, 2].
- Earthquake lights - Even though earthquake lights have been observed in many situations and since the beginning of the last century, doubts persisted in the scientific community [3, 4].
- Ionospheric perturbation - Variations in the Total Electron Content (TEC), registered days before major events suggest the presence of a positive charge on the Earth's surface to which the ionosphere responds [5]. It was later discussed that the release of radon at the Earth's surface causes the stated ionospheric perturbations [6].
- Thermal anomalies – According to infrared (IR) emission studies, there is thermal anomalies occurring before major seismic events. The cause for that to happen has remained mysterious so far [7, 8].
- Low frequency electromagnetic emissions - Low frequency electromagnetic (EM) emissions possibly related to pre-earthquake activity have attracted attention over the past few decades [9, 10]. However, sometimes no EM emissions are registered, which has caused uncertainties amongst the science community [11].

However, we will consider a different point-of-view. Most earthquakes occur in the Earth's crust, which is composed mainly by igneous and high-grade metamorphic rocks. It is of great importance to understand the electrical properties of this kind of rocks.

This research theme covers the study of the structural properties of rocks (e.g., lithology) under specific environmental conditions (e.g., pressure) as well as the study of relationships between structural and mechanical properties (e.g., wave velocities) [12]. The study of temperature effects in this type of research is relatively new, due to the difficulties in creating those conditions [13]. Under the research project AEARAM-FCT, measurements of acoustic emission and electrical signals in

samples subjected to uniaxial pressure and also pre-heated are carried out. This work takes place in the Centro de Geofísica da Universidade de Évora (CGE), the Instituto Superior de Engenharia de Lisboa (ISEL) and the Departamento de Física e Astronomia da Faculdade de Ciências da Universidade do Porto.

So far, there is no satisfactory theoretical model capable of simulating the electrical transport in rocks under mechanical action. Our main objective for this dissertation is to numerically determine, at any stress-strain state of a rock, the space charge distribution and the current-voltage applied characteristic curve.

Rocks are, basically, electrically insulator solid media whose electrical properties can be changed by mechanical action, especially when deformation is accompanied by micro-fracturing processes. We intend to simulate numerically electrical transport in rocks under mechanical action, assuming that electrical charge can be generated by micro-fracturing processes. Atoms that release electrons become positively charged (positive ions) and the released electrons can diffuse and drift across the sample. We consider that the electrical behavior of rocks can be described using an adaptation of the formalism applied to semiconductors, assuming that positive ions have a mobility and diffusion coefficient much smaller than those of free electrons.

1.1. Semiconductors and insulators

Semiconductors are materials where the energy difference between the valence band and the conduction band (band gap), is so narrow that the mean thermal energy is enough to lift electrons from the valence band into the conduction band. For each electron lifted from the conduction band, a hole is left in the valence band. Both act as charge carriers but electrons in the conduction band have much more mobility than holes in the valence band [14].

Insulators present some differences in the width of their band gaps, when compared to semiconductors. In insulators the band gap is so wide that thermal promotion of electrons from valence band into the conduction band becomes practically impossible [14].

Minerals are usually insulators. Holes can exist in silicate minerals, when a site structurally designed for a divalent cation (Fe^{2+}) is occupied by a trivalent cation (Fe^{3+}). In these cases, the hole state tends to be localized on the Fe^{3+} site, meaning that it is not mobile and does not contribute significantly to the conductivity [14].

1.2. Stress-induced activation of electronic charge carriers in rocks

It is known that rocks possess charge carriers in a dormant form [14, 15] and they can be "triggered" with the application of stress. Those charge carriers are known as "positive holes" and they occur in the oxygen anion sublattice. These holes are defect electrons in the O^{2-} sublattice and can be described as O^{-}. When in a dormant state, p-holes exist as spin-paired peroxy bonds that are also known as PHP [14, 16]. When pressure is applied, stress breaks the peroxy bonds and activate p-holes. Then the electrons jumps from the neighboring O^{2-} to the pholes O^{-} and the pholes move out. A phole becomes a highly mobile electronic charge carrier. [14]

1.3. Poisson's equation

The electrostatic potential V created by a charge distribution ρ satisfies Poisson's equation:

$$\boldsymbol{\nabla}^2 V = -\frac{\rho}{\varepsilon} \quad (1)$$

where ε is the electrical permittivity. Assuming that a rock can be treated approximately as a homogeneous and isotropic material, ε is considered to be scalar and constant. As in semiconductor devices, the space charge density ρ can be expressed by [17]:

$$\rho = q(p - n + C) \quad (2)$$

where q is the elementary charge. We assume that rocks exhibit insulator rather than semiconductor behavior, thus p and n are, respectively, the concentrations of positive ions instead of positive ions and electrons; C is the concentration of additional, typically fixed, charges.

In a semiconductor, fixed charges can be originated from charged impurities of donor and acceptor types and from trapped ions or electrons [18]. In the following, however, we will consider an electrically clean rock with no donor or acceptor impurities, nor trapped ions or electrons. In these conditions, $C = 0$ and Poisson's equation can be written as:

$$\boldsymbol{\nabla}^2 V = -\frac{q}{\varepsilon}(p - n) \quad (3)$$

1.4. Current Relations

Charge carriers can move through the lattice by drift under the influence of an electric field and by diffusion due to a concentration gradient.

1.4.1. Carrier drift

Charge carriers subjected to an electric field are accelerated and acquire a certain drift velocity. Positive ions are accelerated in the direction of the electric field $E = -\nabla V$ and electrons in opposite direction. For low electric fields, the drift component of the current density can be expressed in terms of Ohm's law as [19]:

$$\boldsymbol{J_p}^{\boldsymbol{drift}} = \sigma_p \boldsymbol{E} \quad (4a)$$

$$\boldsymbol{J_n}^{\boldsymbol{drift}} = \sigma_n \boldsymbol{E} \quad (4b)$$

Here, σ_p and σ_n denote the electrical conductivity of positive ions and electrons, respectively. In terms of carrier mobility for positive ions μ_p and electrons μ_n, we also have:

$$\sigma_p = qp\mu_p \quad (5a)$$

$$\sigma_n = qn\mu_n \quad (5b)$$

1.4.2. Carrier Diffusion

A concentration gradient of carriers leads to carrier diffusion. This is because of their random thermal motion which is more probable in the direction of the lower concentration. The diffusion current density contributions for both types of charge carriers are written as [19]:

$$\boldsymbol{J_p}^{\boldsymbol{diff}} = qD_p \boldsymbol{\nabla} p \quad (6a)$$

$$\boldsymbol{J_n}^{\boldsymbol{diff}} = -qD_n \boldsymbol{\nabla} n \quad (6b)$$

where D_p and D_n are the diffusion coefficients of positive ions and electrons, respectively. Assuming thermal equilibrium at temperature *T*, we can express the diffusion coefficients in terms of the respective mobilities using the Einstein relation [17]:

$$D_p = \frac{k_B T}{q} \mu_p \quad (7a)$$

$$D_n = \frac{k_B T}{q} \mu_n \quad (7b)$$

where k_B is the Boltzmann constant.

1.4.3. Continuity equations

The total particle current densities include drift and diffusion contributions [19, 20]:

$$\boldsymbol{J}_p = qp\mu_p\boldsymbol{E} - qD_p\nabla p \quad (8a)$$

$$\boldsymbol{J}_n = qn\mu_n\boldsymbol{E} + qD_n\nabla n \quad (8b)$$

The time dependent concentrations of positive ions (*p*) and free electrons (*n*), satisfy the following continuity equations [19]:

$$\frac{\partial p}{\partial t} = -\frac{1}{q}\nabla\cdot\boldsymbol{J}_p + U \quad (9a)$$

$$\frac{\partial n}{\partial t} = \frac{1}{q}\nabla\cdot\boldsymbol{J}_n + U \quad (9b)$$

The quantity $U = G - R_{np}$ is known as the net generation rate; G and R_{np} are the charge generation and recombination rates, respectively. The net-generation rate can be decomposed into an intrinsic contribution (U_i) of Shockley type [21], associated with intrinsic n-p generation and recombination processes, and an extrinsic contribution (U_e) associated with microfracture-induced charge generation to be discussed below:

$$U = U_i + U_e \quad (10a)$$

$$U_i = \frac{np - n_0p_0}{\tau_{np}(n+n_0+p+p_0)} \quad (10b)$$

Here n_0 and p_0 are the equilibrium concentrations of free electrons and positive ions, respectively, and τ_{np} is a characteristic electron-ion recombination time.

1.5. Displacement current

The total current density through the lattice (J_t) includes not only the particle density currents J_p and J_n but also a displacement current density, which, according to Maxwell's theory [20], is given by the time derivative of electrical displacement:

$$J_t = J_p + J_n + \varepsilon\frac{\partial E}{\partial t} \quad (11)$$

1.6. Discretization requirements

The numerical solution of the drift-diffusion equations as described above is stable provided the space and time discretizations satisfy the requirements $\Delta x < L_D$ and $\Delta t < \tau_{dr}$, where the quantities L_D and τ_{dr}, known as the Debye length and the dielectric relaxation time, respectively, are defined by [20]:

$$L_D = \sqrt{\frac{\varepsilon k_B T}{q^2}} \tag{12a}$$

$$\tau_{dr} = \frac{\varepsilon}{\sigma} \tag{12b}$$

Chapter 2

Methods

2.1. Finite difference method

To simulate electrical transport in rocks using the drift-diffusion model, we need to solve partial differential equations, and the three most common methods are the finite element (FEM), the finite volume (FVM) and finite difference method (FDM) [22]. The FDM discretizes time and space domains and applies local Taylor expansions to approximate derivatives. This method is easily implemented in the present model and leads to a system of nonlinear equations with simple Jacobian structure that can be efficiently solved by Gauss-Seidel and Newton's techniques [13].

Because of time limitations, we will apply the FDM only to a one dimensional (1D) lattice. Let $u(x,t)$ be a space (x) and time (t) dependent quantity. Lattice nodes have abscissae $x_i = i\Delta x$ and time record is composed of time instants $t^n = n\Delta t$, where Δx and Δt are, respectively, the space and time discretization spacings. Using the notation $u_i^n \equiv u(x_i, t^n)$, we may write a time partial derivative using a forward finite difference approximation [22]:

$$\frac{\partial u}{\partial t} \approx \frac{u_i^{n+1} - u_i^n}{\Delta t} \tag{13}$$

Space partial derivatives are given by centered approximations:

$$\frac{\partial u}{\partial x} \approx \frac{u_{i+1}^n - u_{i-1}^n}{2\Delta x} \tag{14a}$$

$$\frac{\partial^2 u}{\partial x^2} \approx \frac{u_{i+1}^n - 2u_i^n + u_{i-1}^n}{(\Delta x)^2} \tag{14b}$$

2.2. Gauss-Seidel method - Successive over relaxation scheme

To solve Poisson's equation, we used the Gauss-Seidel method with the successive over relaxation scheme. It is an iterative method useful to solve quadratic systems of linear equations of the type $Ax = B$ [23].

$$A_{\mathrm{i}1}x_{\mathrm{i}} + A_{\mathrm{i}2}x_{\mathrm{i}+1} + A_{\mathrm{i}3}x_3 + \cdots + A_{\mathrm{i}n}x_n = B_{\mathrm{i}} \tag{15}$$

Like in the Jacobi method [9], we isolate the pivots of the matrix, and start with an initial guess of $x_i = 0$. Unlike the Jacobi method, however, Gauss-Seidel iteration, calculates, at each iteration step,

the value of each variable using the newly updated values of the remaining variables:

$$x_i^{iter} = \frac{1}{A_{ii}}\left[B_i - \sum_{j=1}^{i-1} A_{ij}x_j^{iter} - \sum_{j=i+1}^{i-1} A_{ij}x_j^{iter-1}\right] \quad (16)$$

This makes Gauss-Seidel method comparatively faster than Jacobi method [23]. The successive over relaxation scheme is an even faster method and is able to get to the result with less iterations. It takes into account that the convergence of the Gauss-Seidel method can be improved by choosing a linear combination of the old and the actual values and it is stated below:

$$x_i^{iter} = \frac{\omega}{a_{ii}}\left[B_i - \sum_{j=1}^{i-1} a_{ij}x_j^{iter} - \sum_{j=i+1}^{i-1} a_{ij}x_j^{iter-1}\right] + (1-\omega)x_i^{iter-1} \quad (17)$$

where, ω is the relaxation parameter, which depends on the grid spacing, boundary conditions imposed and geometrical shape of the domain. Typical values of ω are between 0 and 2, and must be chosen so that the rate of convergence is maximized [23].

2.3. Scharfetter-Gummel scheme

Assuming the one dimensional case, a rock sample of length L_x, can be modelled as a discrete 1D lattice of $N+1$ nodes at the positions $x_i = i \cdot \Delta x$, where $\Delta x = L_x/N$ is the lattice spacing. In order to discretize the continuity equations, we need to calculate the currents at points between lattice nodes. The solutions are only available in the nodes, which means that interpolation schemes are necessary to calculate the currents. The Scharfetter-Gummel scheme is one of the most used ways to discretize the drift-diffusion equation in semiconductors and provides an optimal solution to this problem [24].

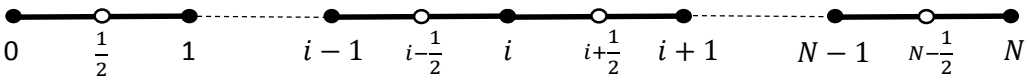

Fig. 1 – Sharfetter-Gummel scheme diagram.

The quantities $p(x)$, $n(x)$, $V(x)$, $G(x)$ and $R(x)$ are all defined at the lattice nodes: $p(x_i) \equiv p_i$, $n(x_i) \equiv n_i$, $V(x_i) \equiv V_i$, $G(x_i) \equiv G_i$, $R(x_i) \equiv R_i$. On the other hand, variables $J_p(x)$, $J_n(x)$ and $E(x)$ are defined at the midpoints between adjacent nodes: $J_p(x_{i\pm\frac{1}{2}}) \equiv J_{p|i\pm\frac{1}{2}}$, $J_n(x_{i\pm\frac{1}{2}}) \equiv J_{n|i\pm\frac{1}{2}}$, $E(x_{i\pm\frac{1}{2}}) \equiv E_{i\pm\frac{1}{2}}$.

The drift-diffusion model is characterized by the set of coupled equations in the variables $p(x,t)$, $n(x,t)$ and $V(x,t)$ [20]:

Continuity equations:

$$\frac{\partial p}{\partial t} = -\frac{1}{q}\frac{\partial J_p}{\partial x} + U \tag{17a}$$

$$\frac{\partial n}{\partial t} = \frac{1}{q}\frac{\partial J_n}{\partial x} + U \tag{17b}$$

Current equations:

$$J_p = q\mu_p pE - qD_p\frac{\partial p}{\partial x} \tag{17c}$$

$$J_n = q\mu_n nE + qD_n\frac{\partial n}{\partial x} \tag{17d}$$

Poisson's equation:

$$\frac{\partial^2 V}{\partial x^2} = \frac{q}{\varepsilon}(n - p) \tag{17e}$$

Electric field equation:

$$E = -\frac{\partial V}{\partial x} \tag{17f}$$

From equation 17c and 17d, we have [20, 25]:

$$\frac{\partial p}{\partial x} = ap - \frac{J_p}{qD_p} \tag{18a}$$

$$\frac{\partial n}{\partial x} = bp - \frac{J_n}{qD_n} \tag{18b}$$

where $a = \frac{\mu_p E}{D_p}$ and $b = \frac{\mu_n E}{D_n}$. It is common to assume that *V* varies linearly between adjacent nodes, which means that the electric field is constant between x_i and x_{i+1}. In the Scharfetter-Gummel scheme [26], $\mu_{p,n}$, $D_{p,n}$, $\boldsymbol{J_{p,n}}$ are also assumed constant between the lattice nodes, The concentration of positive ions and electrons in the mid-points, however, are not, in general, an average of the values in the two neighboring nodes. The concentrations $n(x)$, $p(x)$ satisfy the conditions: $n(x_i) = n_i$, $n(x_{i+1}) = n_{i+1}$, $p(x_i) = p_i$, $p(x_{i+1}) = p_{i+1}$. After integration of equation 18a and 18b, we have:

$$J_{p\,i+\frac{1}{2}} = -\frac{qD_p}{\Delta x_i}\left[\left(\frac{a\Delta x_i}{(e^{a\Delta x_i}-1)}\right)p_{i+1} - \left(\frac{-a\Delta x_i}{(e^{-a\Delta x_i}-1)}\right)p_i\right] \tag{19a}$$

$$J_{n\,i+\frac{1}{2}} = \frac{qD_n}{\Delta x_i}\left[\left(\frac{b\Delta x_i}{(e^{b\Delta x_i}-1)}\right)n_{i+1} - \left(\frac{-b\Delta x_i}{(e^{-b\Delta x_i}-1)}\right)n_i\right] \tag{19b}$$

where $\Delta x_i = x_{i+1} - x_i$.

Finally we obtain [20]:

$$J_{p_{i+\frac{1}{2}}} = -\frac{qD_p}{\Delta x_i}\left[B\left(y_{p_i}\right)p_{i+1} - B\left(-y_{p_i}\right)p_i\right] \quad (20a)$$

$$J_{n_{i+\frac{1}{2}}} = \frac{qD_n}{\Delta x_i}\left[B\left(y_{n_i}\right)n_{i+1} - B\left(-y_{n_i}\right)n_i\right] \quad (20b)$$

where $y_{p_i} = -(V_{i+1} - V_i)/V_T$, $V_T = K_B T/q = D_p/\mu_p$ and $B(y)$ is the Bernoulli function defined by:

$$B(y) = \frac{y}{e^y - 1} \quad (21)$$

Chapter 3

Numerical solution of 1D drift-diffusion equations

3.1. Model parameters

In the simulation, we considered a lattice of length $L_x = 1.0$ m and spacing $\Delta x = 0.002$ m, corresponding to a total of 501 nodes. The lattice dimensions along y (L_y) and z (L_z) directions are both $0.1\ m$. The discretization time Δt is equal to $1\ \mathrm{m}s$. The value of the electrical permittivity of the rock is ten times the value of electrical permittivity of vacuum ($\varepsilon = 10\varepsilon_0$), which is a typical value for rocks such as granite. The equilibrium intrinsic concentrations of electrons and positive ions are equal to 10^{12} (m^{-3}) and the values chosen for the mobility of electrons and positive ions are $10^{-4}\ m^3.V^{-1}.s^{-1}$ and $10^{-7}\ m^3.V^{-1}.s^{-1}$, respectively. The intrinsic carrier concentration and mobility were chosen in order to ensure the discretization requirements [20]. The characteristic electron-ion recombination time is $\tau_{np} = 5.0$ s. The end nodes $(0, N)$, as seen in fig. 1, are subjected to Dirichlet boundary conditions:

$$V_0 = V_{app} \tag{22a}$$

$$V_N = 0 \tag{22b}$$

3.2. Discretization of Poisson's equation

Using finite differences, Poisson's equation can be approximated as follows [20]:

$$\left(\frac{\partial^2 V}{\partial x^2}\right)_{x_i} \approx \frac{V_{i+1}-2V_i+V_{i-1}}{(\mathrm{d}x)^2} = -\frac{q}{\varepsilon}(p_i - n_i) \tag{23a}$$

$$V_{i+1} - 2V_i + V_{i-1} = -\frac{q(\mathrm{d}x)^2}{\varepsilon}(p_i - n_i) \tag{23b}$$

This system of equations for $i = 1, \cdots, N-1$ can be solved using the Gauss-Seidel iteration method with over relaxation:

$$V_i^{iter} = \frac{\omega}{2}\left[\sum_{j=1}^{i-1} V_j^{iter} + \sum_{j=i+1}^{i-1} V_j^{iter-1} + \frac{q(\mathrm{d}x)^2}{\varepsilon}(p_i - n_i)\right] + (1-\omega)V_i^{iter-1} \tag{24}$$

where $\omega \approx 1.9$ is the relaxation parameter.

Given the values of the concentrations n_i and p_i, the potentials V_i $(i = 1, \ldots N)$ can be determined iteratively using Gauss-Seidel method with over relaxation. The iteration proceeds until a predefined

maximum number of iterations is reached, or the maximum potential change between consecutive iteration steps becomes smaller than a predefined potential tolerance.

There is also the possibility of setting V_{app} as a harmonic function of time, with amplitude A_V, bias V_0 and angular frequency w:

$$V_{app}(\mathrm{t}) = V_0 + A_V \sin(wt) \tag{25}$$

3.3. Discretization of current equations

The discretized representation of the total current density J_t is given by:

$$J^k_{t|i+\frac{1}{2}} = J^k_{p|i+\frac{1}{2}} + J^k_{n|i+\frac{1}{2}} + \frac{\varepsilon}{\Delta t}\left(E^k_{i+\frac{1}{2}} - E^{k-1}_{i+\frac{1}{2}}\right) \tag{26a}$$

where the electric field is calculated from the potential through a second order (in Δx) approximation:

$$E^k_{i+\frac{1}{2}} = \frac{V^k_{i+1} - V^k_i}{\Delta x} \tag{26b}$$

3.4. Discretization of continuity equations

The continuity equations are discretized using the Scharfetter-Gummel conservative scheme:

$$\frac{p^{k+1}_i - p^k_i}{\Delta t} \approx -\frac{J^k_{p|i+\frac{1}{2}} - J^k_{p|i-\frac{1}{2}}}{q\Delta x} + U^k_i \tag{27a}$$

$$\frac{n^{k+1}_i - n^k_i}{\Delta t} \approx \frac{J^k_{n|i+\frac{1}{2}} - J^k_{n|i-\frac{1}{2}}}{q\Delta x} + U^k_i \tag{27b}$$

$$p^{k+1}_i \approx p^k_i - \frac{\Delta t}{q\Delta x}\left(J^k_{p|i+\frac{1}{2}} - J^k_{p|i-\frac{1}{2}}\right) + \Delta t U^k_i \tag{27c}$$

$$n^{k+1}_i \approx n^k_i + \frac{\Delta t}{q\Delta x}\left(J^k_{n|i+\frac{1}{2}} - J^k_{n|i-\frac{1}{2}}\right) + \Delta t U^k_i \tag{27d}$$

The concentration of electrons and positive ions, satisfy the following initial and boundary conditions:

$$p^0_i = n^0_i = p_0 = 10^{12}\ m^{-3} \tag{28a}$$

$$p^k_0 = p^k_N = n^k_0 = n^k_N = 10^{12}\ m^{-3} \tag{28b}$$

3.5. Extrinsic generation rate

The extrinsic charge generation rate (U_e) depends on the time evolution of micro-fracture events, which is dictated by the stress-strain history. In a simplified approach, we can assume a deterministic time-dependent distribution of charge generation events.

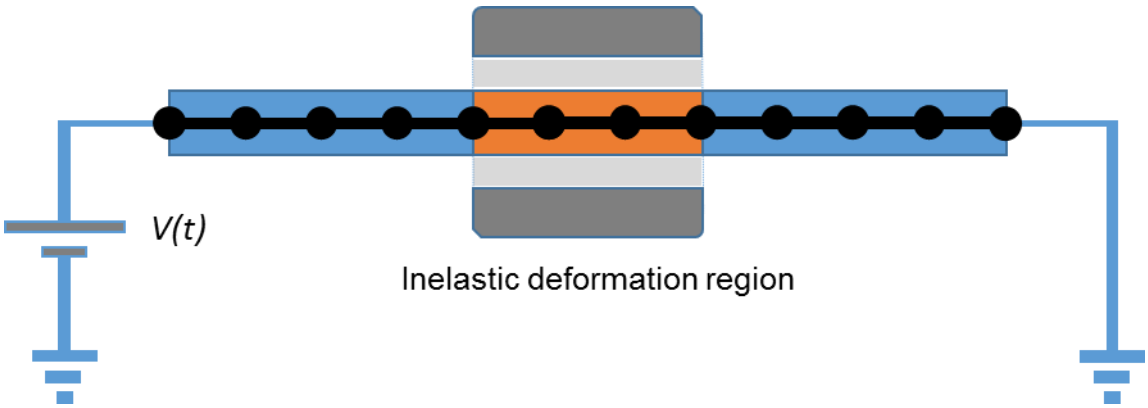

Fig. 2: Representation of uniaxial compressing geometry. Inelastic deformation region (orange zone).

For uniaxial compressing geometry, the sample region between pistons is the region where the deformation is more concentrated and thus it is also the sample region most affected by fracture (fig. 2). For this reason, we assume that fracture-induced charge generation is described by a generation rate function $G(x,t)$ whose spatial dependence is concentrated in the deformation region. Several particular forms of $G(x,t)$ can be used to describe different phenomena and/or simulation regimes:

a. Time pulse uniform in the deformation region:

$$G(x,t) = A \cdot [H(x - x_{drl}) - H(x - x_{drr})] \cdot \left[H(t - t_{ini}) - H(t - t_{fin})\right] \qquad (29a)$$

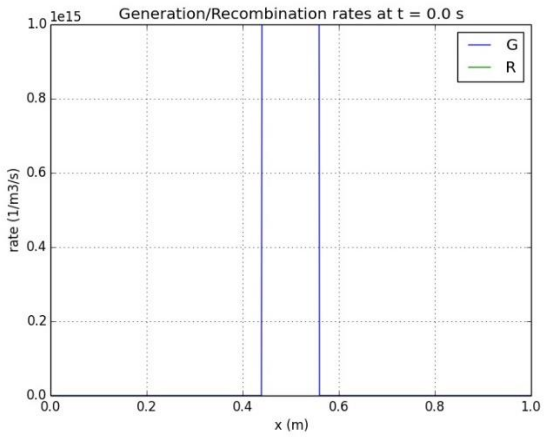

Fig. 3a: Generation function plot for t = 0.0 s.

b. Gaussian time pulse and Gaussian in the deformation region:

$$G(x,t) = Ae^{-\left(\frac{x-x_c}{2\sigma_x}\right)^2} e^{-\left(\frac{t-t_c}{2\sigma_t}\right)^2} \quad (29b)$$

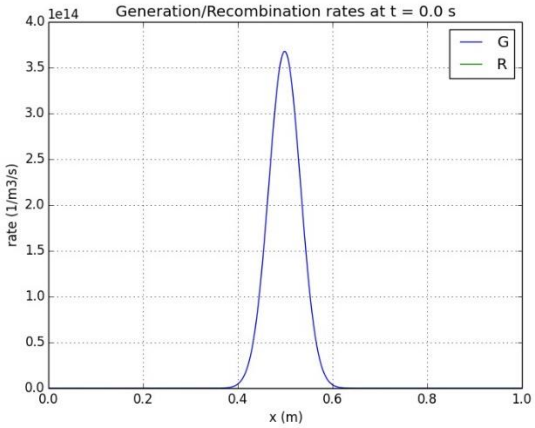

Fig. 3b: Generation function plot for *t* = 0.0 s.

c. Exponential time decay and Gaussian in the deformation region:

$$G(x,t) = Ae^{-\left(\frac{x-x_c}{2\sigma_x}\right)^2} e^{-\frac{t}{\tau}} \quad (29c)$$

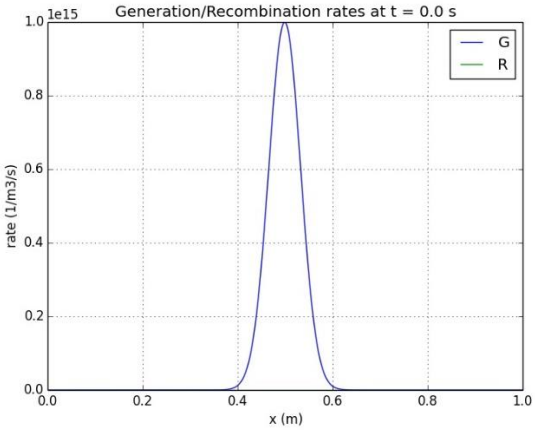

Fig. 3c: Generation function plot for *t* = 0.0 s.

d. Gaussian time pulse and Gaussian centered in the borders of the deformation region:

$$G(x,t) = A\left[e^{-\left(\frac{x-x_{drl}}{2\sigma_x}\right)^2} + e^{-\left(\frac{x-x_{drr}}{2\sigma_x}\right)^2}\right] e^{-\left(\frac{t-t_c}{2\sigma_t}\right)^2} \quad (29d)$$

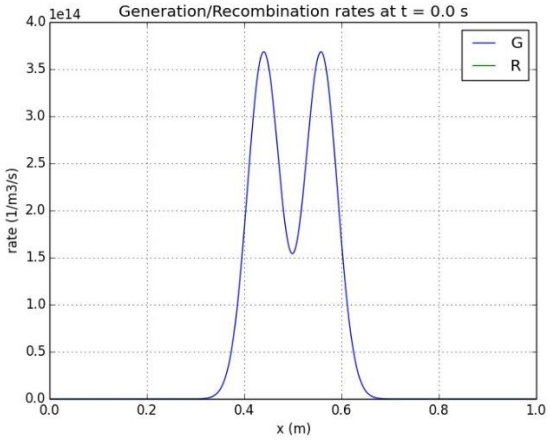

Fig. 3d: Generation function plot for *t* = 0.0 s.

e. Exponential time decay and Gaussian centered in the borders of the deformation region:

$$G(x,t) = A\left[e^{-\left(\frac{x-x_{drl}}{2\sigma_x}\right)^2} + e^{-\left(\frac{x-x_{drr}}{2\sigma_x}\right)^2}\right]e^{-\frac{t}{\tau}} \tag{29e}$$

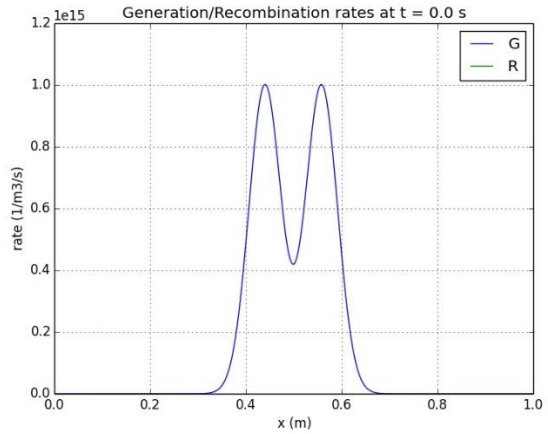

Fig. 3e: Generation function plot for *t* = 0.0 s.

where A is an amplitude factor, $H(x)$ the step Heaviside function and x_{drl}, x_{drr} are, respectively, the left and right borders of the deformation region; t_{ini}.and t_{fin} are the initial and final times of the time pulse; x_c is the center of the deformation region $\left(x_c = \frac{x_{drl}+x_{drr}}{2}\right)$ and σ_x is the half-width of the spatial Gaussian; t_c is the center of Gaussian time pulse and σ_t the corresponding half-width; τ is the time constant of the decay of the generation rate.

In case a) we assume a linearly time dependent amplitude:

$$A(t) = a_0 + a_1 t \tag{30}$$

This function has, however, the disadvantage of being discontinuous in x and t, which introduces unwanted integration errors.

The graphical representations of the generation functions are located in section 4.

3.6. Simulation

In order to run the simulation it was necessary to create a main function which will run every function mentioned in the previous sections. In the first place, it is necessary to create an auxiliary function, which turns the system into equilibrium state by setting the concentration of electrons and ions equal to their intrinsic values. The function also solves the Poisson's equation and determines the electric field. The chosen values for n_0 and p_0 are both equal to $10^{12}m^{-3}$ and Poisson's equation reduces to $\nabla^2 V = 0$ in the equilibrium state.

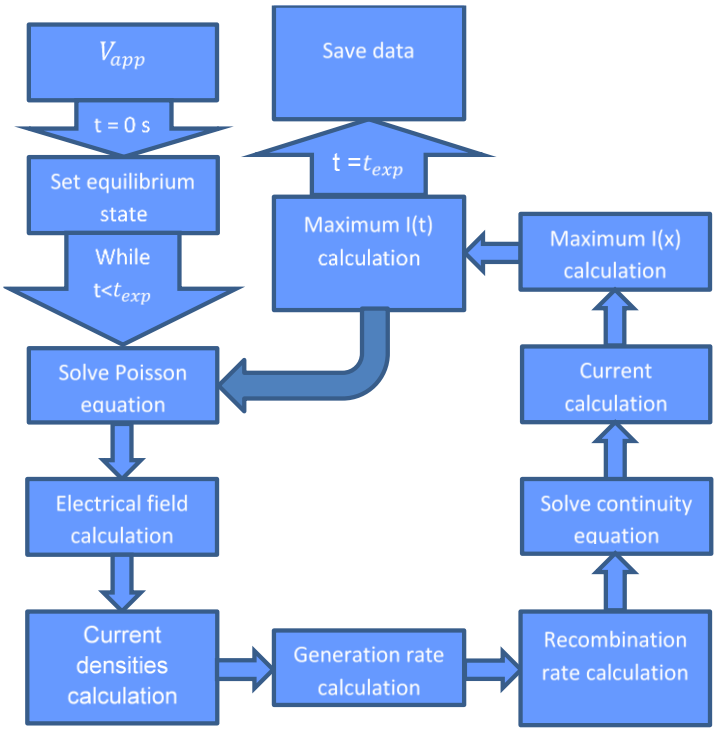

Fig. 4: Flowchart describing the simulation (t_{exp} – time experience).

From the flowchart in fig. 4, it is possible to observe that the function that sets equilibrium state, appears in the first place, then a cycle starting from $t = 0.0$s to $t = t_{exp}$, with intervals of $\Delta t = 1$ ms, calculates the potentials, electrical fields, current densities, generation and recombination rates and charge concentrations. Finally when $t = t_{exp}$ the function, saves all data.

3.7. Current-voltage curve

The current-voltage curve is calculated with various successive simulations using different values of applied potential (V_{app}) and recording the maximum value of the transient current. The current is determined from the values of total current density, and the lattice cross-section area:

$$I_{i+\frac{1}{2}} = J_{t_{i+\frac{1}{2}}} \times L_y \times L_z \quad (31)$$

3.8. Discretization requirements

It is possible to verify that the values of Δx and Δt are much smaller than Debye's length ($L_d \approx 3783$ m) and the dielectric relaxation time ($\tau_{dr} \approx 5.531$ s), respectively, satisfying the discretization requirements.

Chapter 4

Results and analysis

After some preliminary tests with the algorithm, we were able to understand which parameters should be chosen in order to study the generation and recombination rates, the variation in the concentration of ions and electrons, and the $I(V)$ curve. In order to understand the generation rate function, we need to look at the initial moments of the simulation. However, the observation of $n(x)$, $p(x)$ and $R(x)$, requires more time of experience, especially in section 4.1.1, where the generation rate function is a pulse function. Because of that, it was also necessary to increase the number of nodes to 1001 instead of 501 nodes, for a proper analysis of the generation function G_a.

In all examples of chapter 4, the maximum values of current occur in the beginning of the simulation. So, in order to determine the $I(V)$ curve, we choose a lower value of t_{exp}, and set the number of iterations to 10 000, to have the best possible results. The following results were registered with temperature $T = 300$ K.

4.1. Constant applied potential

We considered two different values of applied voltage, 0V and 20V, and except for the first subsection 4.1.1, where $t_{exp} = 1.0$ s (in order to better observe the behavior due to its pulse response), the time of simulation is equal to 0.25 s. Some graphs are not presented in subchapter 4.1.1, mainly due to the difficulties in observing the behavior of the current densities. Only the corresponding maximum values are available and the moments where they occur.

4.1.1. Time pulse uniform in the deformation region (G_a)

It is possible to verify by fig. 5 that, although V_{app} is zero for values of x between 0.44 m and 0.56 m (which corresponds to the deformation region), a stepwise increase in potential occurs due to carrier generation rate (fig. 6), which has been set in this range as:

$$G_a = 10^{12} + 10^7 t, \quad \text{for} \quad (t \leq 2 \text{ ms}) \quad \text{and} \quad G_a = 0, \quad \text{for} \quad (t > 2 \text{ ms}) \qquad (32a)$$

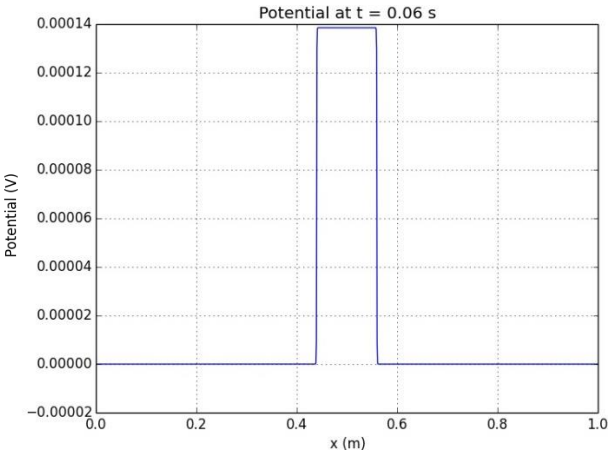

Fig. 5: $V(x)$ plot for $Vapp = 0.0V$ and $t = 60$ ms.

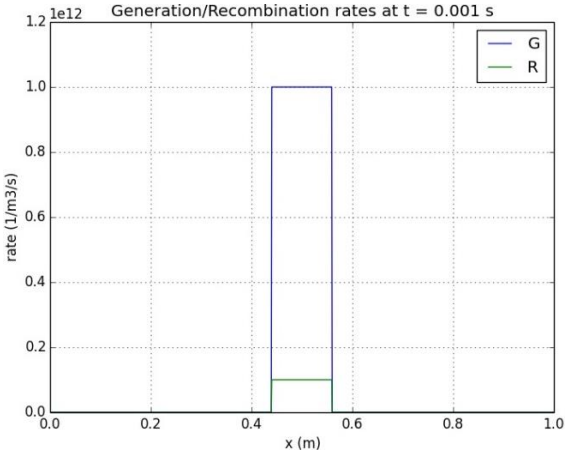

Fig. 6: $G_a(x)$ and $R(x)$ plot for $t = 1$ ms.

The maximum value of electric field is reached for $t = 40$ ms, as seen in the figure 7a and 7b for $V_{app} = 0.0$ V and $V_{app} = 20.0$ V, respectively:

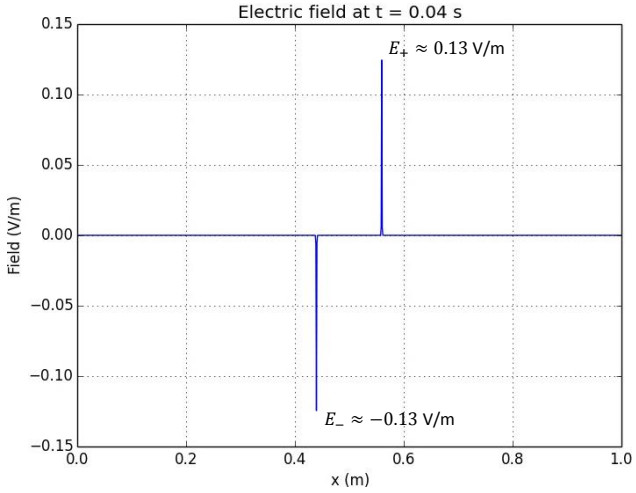

Fig. 7a: $E(x)$ plot for $V_{app} = 0.0$ V for t = 40 ms.

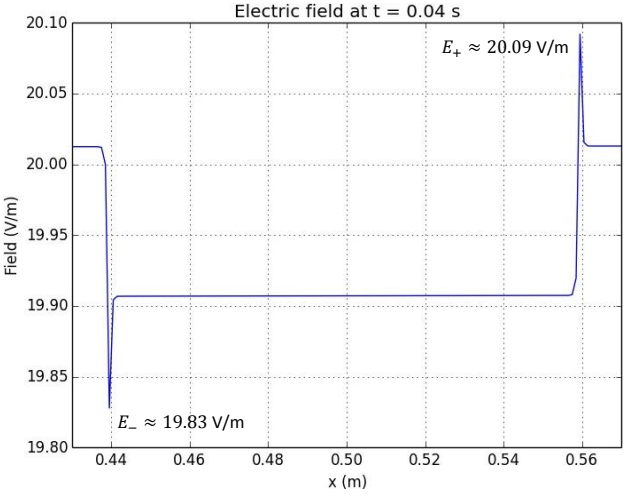

Fig. 7b: $E(x)$ plot for $V_{app} = 20.0$ V for t = 40 ms.

The recombination reaches its maximum value of ~2.7 x 10^{11} $m^{-3}s^{-1}$ for t = 3 ms, after the generation rate pulse given by equation (32), as seen in fig. 8. From that time to the end of simulation, the recombination rate decays to zero.

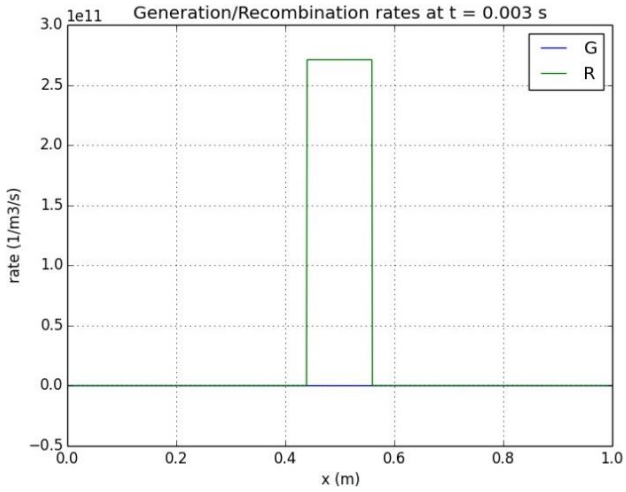

Fig. 8: $G_a(x)$ and $R(x)$ plot for t = 3 ms.

Due to the type of generation rate function, which is a pulse function, the variation of generation and recombination rates is concentrated in a very small fraction of the sample, as we can see from fig. 9a for t = 1.0 s. A zoomed plot of the region between DR_L and DR_R is represented in fig. 9b, and we can observe a lower recombination as compared to fig. 8. It is also possible to realize from fig. 9b, the problems that low discretization may present. In this simulation we considered t_{exp} = 1.0 s, in order to be able to understand the behavior of the curves.

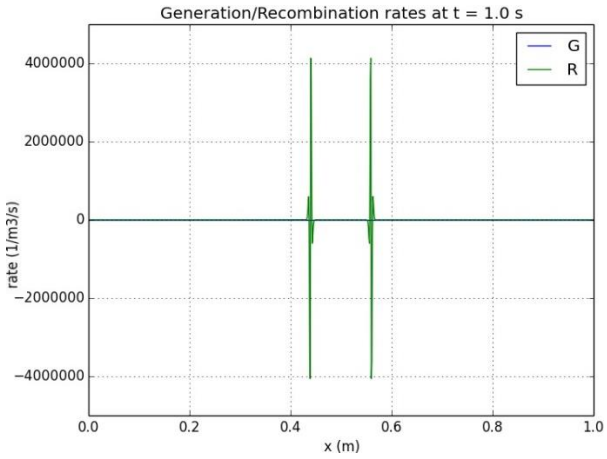

Fig. 9a: $R(x)$ plot for V_{app} = 0.0 V.

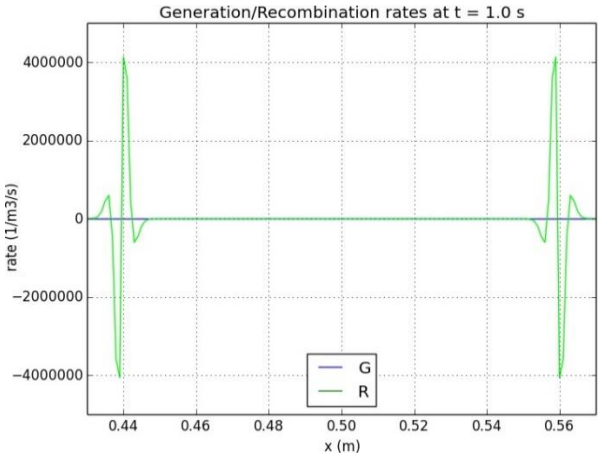

Fig. 9b: $R(x)$ zoomed plot V_{app} = 0.0 V.

From the data registered in fig. 9b and fig. 10b, we can see an increase of the recombination rate with the increase of V_{app}. The recombination rate for V_{app} = 20.0 V is almost double than that for V_{app} = 0.0 V at t = 1.0 s.

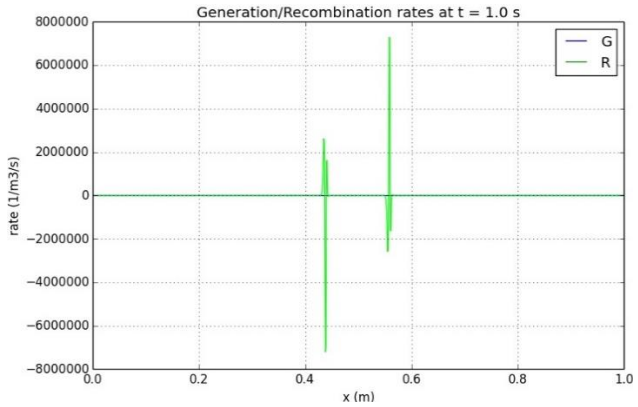

Fig. 10a: R(x) plot for $Vapp = 20.0$ V and $t = 1.0$ s.

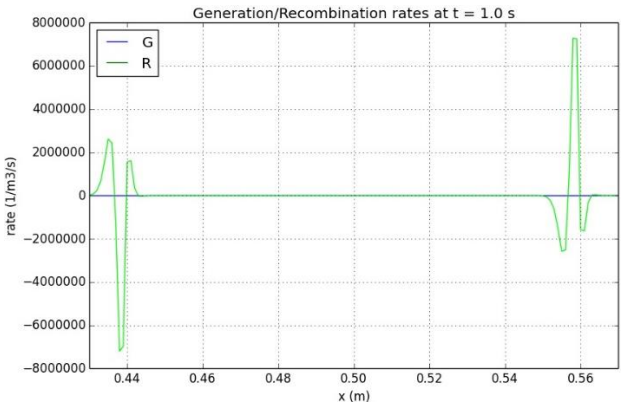

Fig. 10b: R(x) zoomed plot for $Vapp = 20.0$ V and $t = 1.0$ s.

As previously stated, the variation of $n(x)$ (blue line) and $p(x)$ (green line) is concentrated in a very small fraction of the sample (fig.11a). We cannot see the evolution of $n(x)$, $p(x)$ and $\rho(x)$ (red line) properly; however it is possible to see that the concentrations of electrons and positive ions only change in the limits of the deformation region.

In fig. 11b, we show a zoomed plot, where it is apparent that a smaller lattice spacing would be desirable. The maximum variation of the concentrations of electrons and positive ions is ~ 0.32 %.

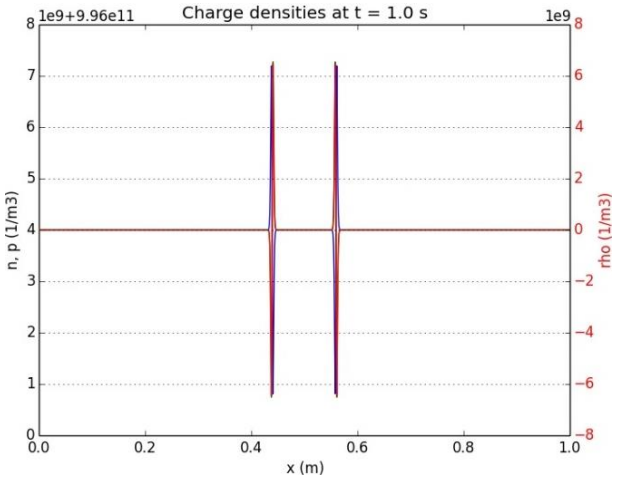

Fig. 11a: $n(x)$, $p(x)$ and $\rho(x)$ plot, for $Vapp = 0.0$ V.

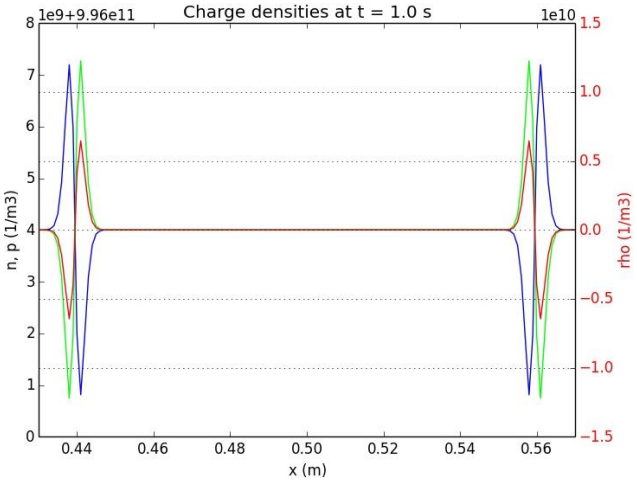

Fig. 11b: $n(x)$, $p(x)$ and $\rho(x)$ zoomed plot, for $Vapp = 0.0$ V.

Comparing the results from fig. 12a and fig. 12b with the previous plots, we can see an increase in the variation of $n(x)$ and $p(x)$. The oscillation of the concentrations of electrons and positive ions is directly related to the value of V_{app}. In this case, the maximum variation of $n(x)$ and $p(x)$ is ~ 0.8 %.

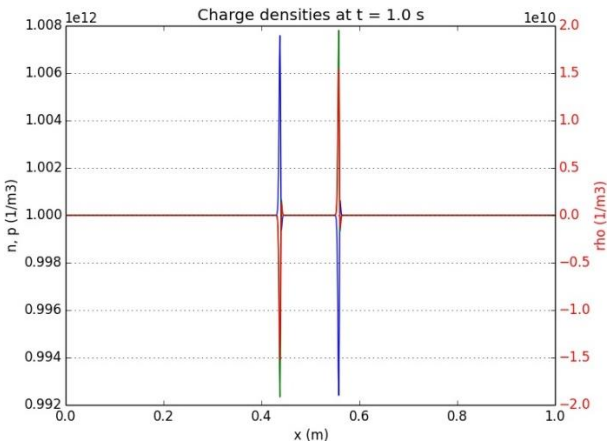

Fig. 12a: $n(x)$, $p(x)$ and $\rho(x)$ plot, for $Vapp = 20.0$ V.

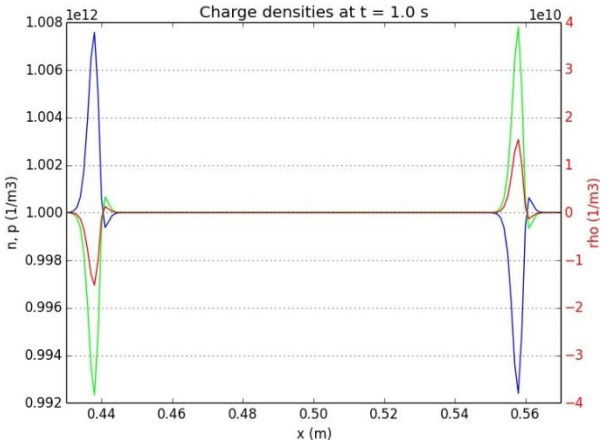

Fig. 12b: $n(x)$, $p(x)$ and $\rho(x)$ zoomed plot, for $Vapp = 20.0$ V.

The maximum values of n(x), p(x) and ρ(x) obtained for $V_{app} = 0.0$ V were as follows:

- $n(x) \approx 3.7\times 10^{12}\ m^{-3}$ for $t = 2$ ms;
- $p(x) \approx 3.7\times 10^{12}\ m^{-3}$ for $t = 2$ ms;
- $\rho(x) \approx \pm\ 6.5\times 10^{10}\ m^{-3}$ for $t = 30$ ms

The maximum values of current densities obtained for $V_{app} = 0.0$ V were as follows:

- $J_t(x) \approx \pm$ 400 pA.m^{-2} for $t = 1$ ms;
- $J_n(x) \approx \pm$ 1100 pA.m^{-2} for $t = 3$ ms;
- $J_d(x) \approx \pm$ 1100 pA.m^{-2} for $t = 4$ ms;
- $J_{n,d}(x) \approx \pm$ 25 pA.m^{-2} for $t = 70$ ms.

The ion current density exhibits much lower values when compared to the other components of the current densities. $J_t(x)$ reaches the highest value for $t = 1$ ms and after that event it decreases. However, the other two components of total current density, $J_n(x)$ and $J_d(x)$, behave differently. After reaching the initial maximum peak ($t = 4$ ms), they decrease in value and it is possible to observe current reverse polarity at $t \approx 40$ ms ($J_{n,d}(x) \approx \pm 14$ pA.m^{-2}). It is possible to see a new increase in value until they reach a local maximum ($J_{n,d}(x) \approx 25$ pA.m^{-2}) at $t \approx 70$ ms. Then $J_n(x)$ and $J_d(x)$ fade away on approach to equilibrium state.

In fig. 13a and fig. 13b, we can see zoomed plots of the current densities at *t* = 1.0 s for $V_{app} = 0.0$ V and $V_{app} = 20.0$ V, respectively.

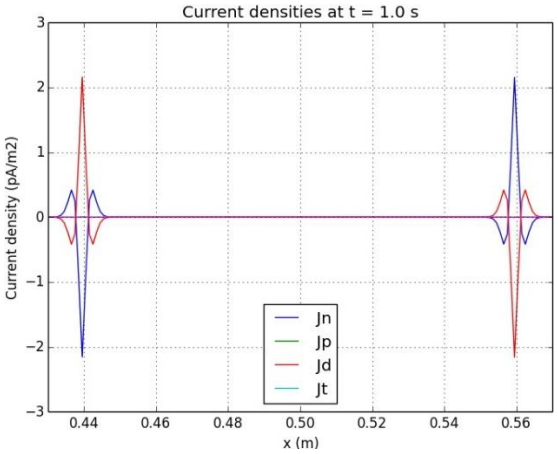

Fig. 13a: Current densities plot for $Vapp = 0.0$ V and $t = 1$ s.

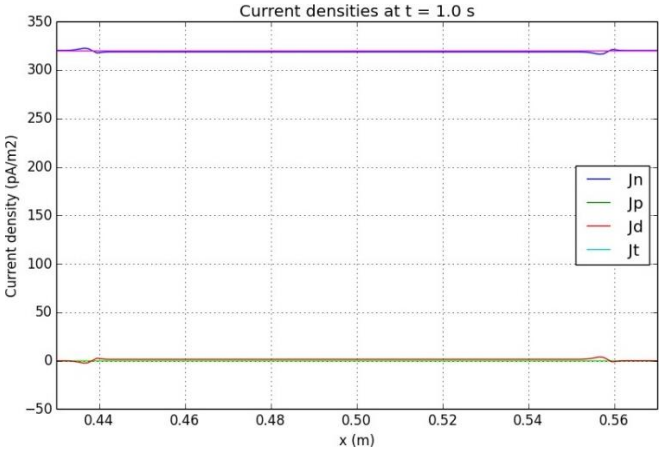

Fig. 13b: Current densities plot for $Vapp = 20.0$ V and $t = 1$ s.

In fig. 14, it is represented the current versus potential applied curve which shows that the current increases almost linearly with the increase of V_{app}. The increase can be considered linear and it is defined by $I = 2.09 \times 10^{-10} V_{app} + 1.00 \times 10^{-12}$ (A) with degree of correlation equal to 1.0.

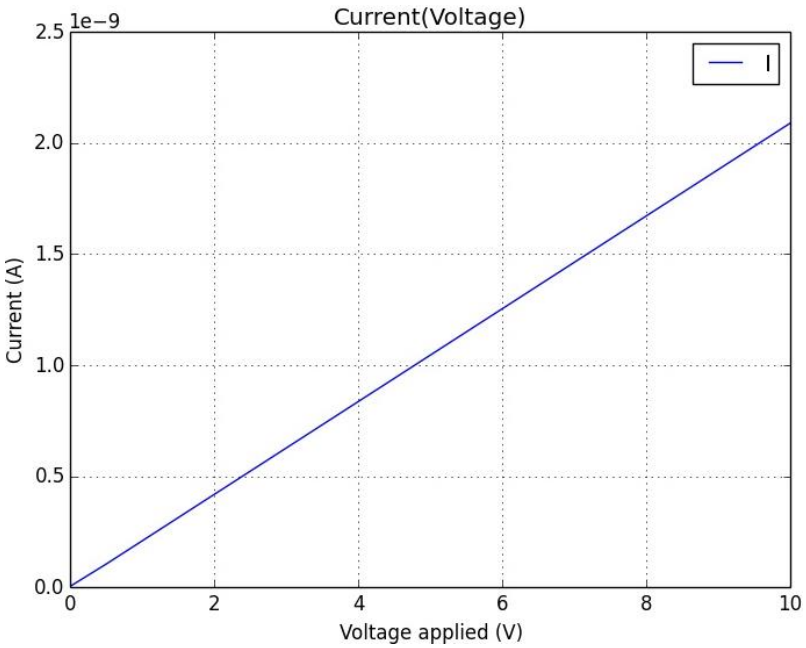

Fig. 14: $I(Vapp)$ plot.

4.1.2. Gaussian time pulse and Gaussian in the deformation region (G_b)

It is possible to observe, in fig.15, the variation of potential, for $V_{app} = 0.0$ V, reaching a peak of ~ 63 mV at t ≈ 60 ms, caused by the Generation rate function G_b represented in fig. 16, and defined as:

- $A = 10^{15}\ m^{-3}s^{-1}$
- $t_c = 2$ ms
- $x_c \approx 25$ cm
- $\sigma_x \approx 2.4$ cm
- $\sigma_t = 1$ ms

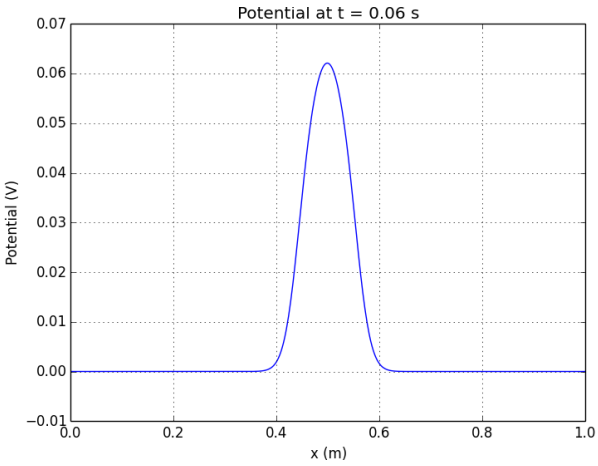

Fig. 15: $V(x)$ plot with applied potential of 0V and t = 60 ms.

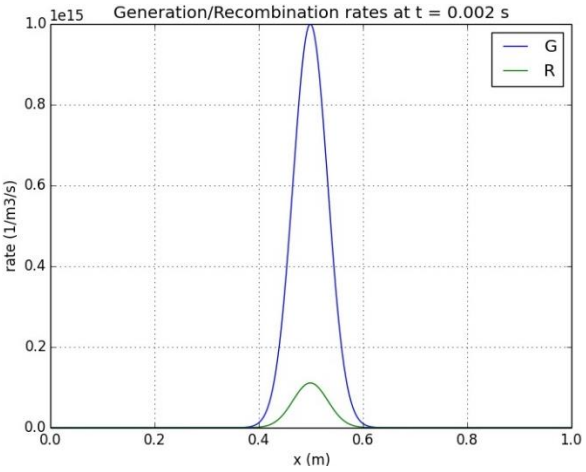

Fig. 16: $G(x)$ and $R(x)$ plot for $t = 2$ ms.

The electric field registered the maximum values for t ≈ 60 ms, with applied voltage equal to 0.0 V and 20.0 V (fig. 17a and fig. 17b).

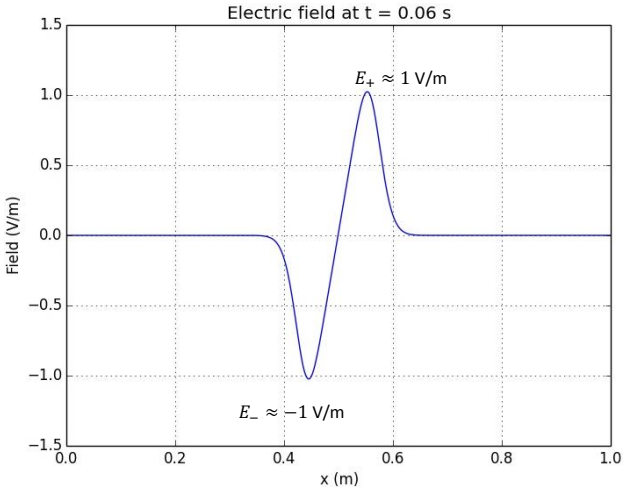

Fig. 17a: $E(x)$ plot for $Vapp = 0.0$ V and $t = 60$ ms.

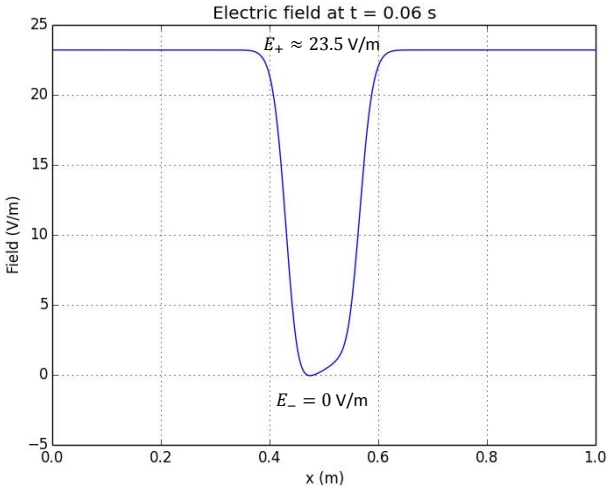

Fig. 17b: $E(x)$ plot for $Vapp = 20.0$ V and $t = 60$ ms.

The generation rate rises until it reaches its maximum value ($G_b = 10^{15}\ m^{-3}s^{-1}$) at t = 2 ms (fig. 16) and then decreases to zero in a very short amount of time (t ~ 10 ms). The recombination rate increases its value until t = 4 ms reaching a maximum peak of $\sim 2.7 \times 10^{14}\ m^{-3}s^{-1}$ (fig. 18a). After that time, $R(x)$ decreases. These results are independent of the applied voltage.

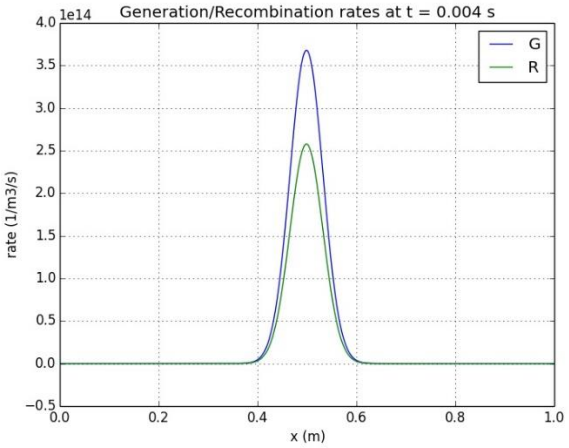

Fig. 18a: Plot with the maximum value of recombination rate for $Vapp = 0.0$ V.

The two images below show the recombination rate evolution, for $V_{app} = 0.0$ V and $V_{app} = 20.0$ V. For nonzero values of V_{app}, the shape of the $R(x)$ curve changes (for $t \approx 150$ ms), and the value of recombination rate increases, with the increase of V_{app}, as we can see in fig. 17c, which shows the type of curve that the recombination rate exhibits with $V_{app} = 20.0$ V. The recombination, for $V_{app} = 20.0$ V is almost the double when compared to the case where $V_{app} = 0.0$ V.

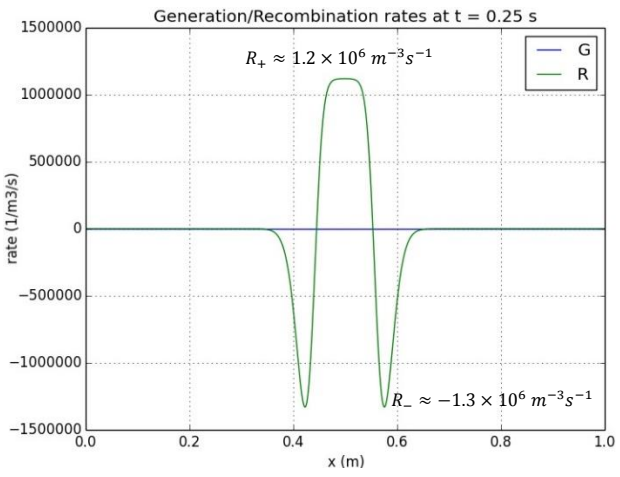

Fig. 18b: Plot of recombination rate evolution with $Vapp = 0.0$ V.

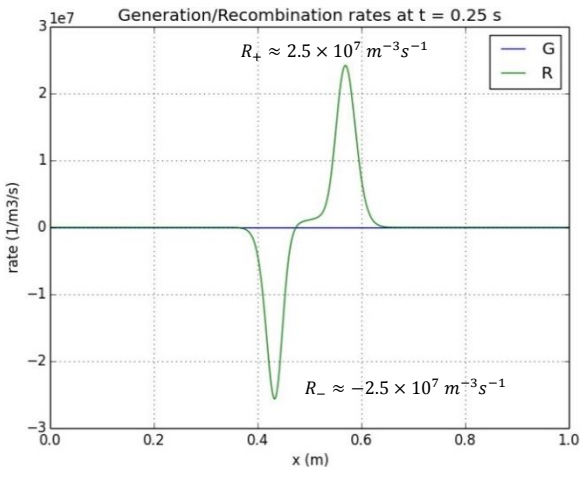

Fig. 18c: Plot of R(x) evolution with $Vapp = 20.0$ V.

The maximum values of $n(x)$ and $p(x)$ were obtained for $t = 4$ ms (fig. 19a), and the highest value of $\rho(x)$ was registered for $t \approx 30$ ms (fig. 19b).

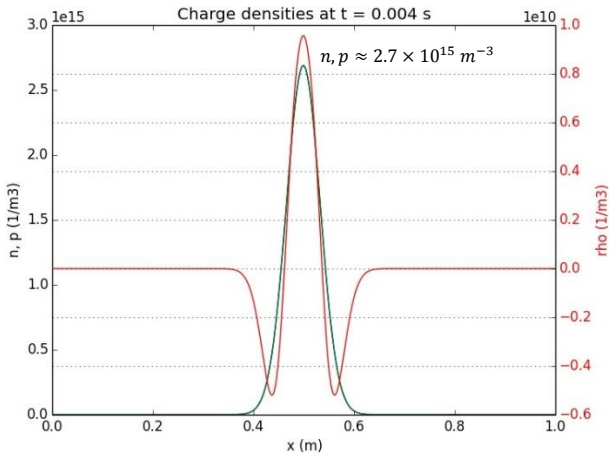

Fig. 19a: $n(x)$, $p(x)$ and $\rho(x)$ plot for $Vapp = 0.0$ V and $t = 4$ ms.

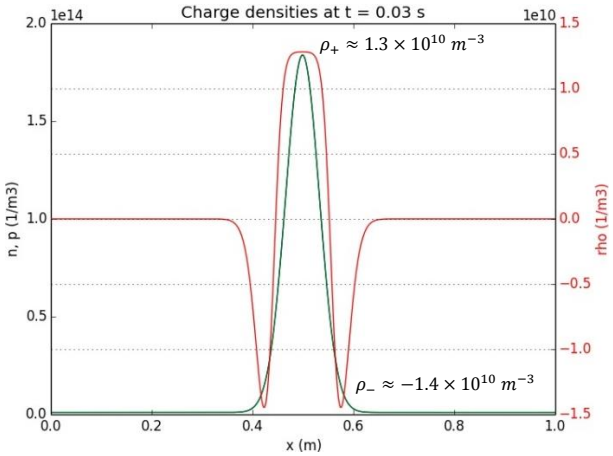

Fig. 19b: $n(x)$, $p(x)$ and $\rho(x)$ plot for $Vapp = 0.0$ V and $t = 30$ ms.

It is possible to verify some variations between $t \approx 100$ ms and $t \approx 130$ ms. The final shape of $n(x)$ and $p(x)$ is represented below (fig. 20a and fig. 20b).

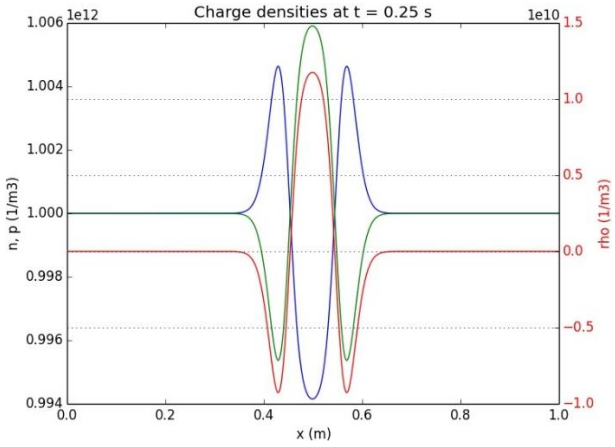

Fig. 20a: $n(x)$, $p(x)$ and $\rho(x)$ plot for $Vapp = 0.0$ V.

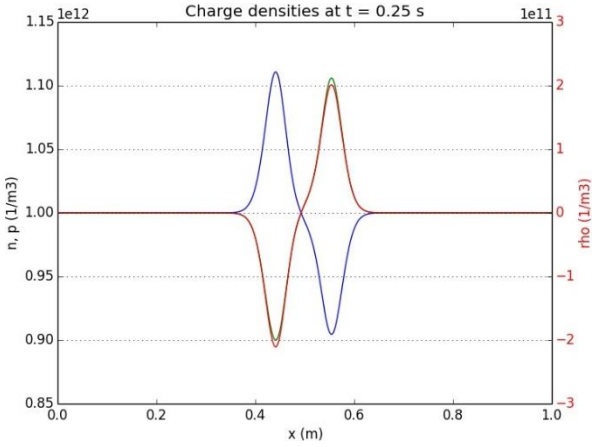

Fig. 20b: $n(x)$, $p(x)$ and $\rho(x)$ plot for $Vapp = 20.0$ V.

Looking at fig. 20a, we can see that for $V_{app} = 0.0$ V there is a smaller oscillation of the value of ρ when compared with fig. 20b for $V_{app} = 20.0$ V, due to the fact that the oscillation of values of concentration of electrons and positive ions, increases with the increase of V_{app} as stated in G_a. In fig. 20a it is possible to verify that $n(x)$ and $p(x)$ vary a maximum of 0.6 %, and in fig. 20b, the values oscillates less than 11 %.

The maximum values of current densities obtained for $V_{app} = 0.0$ V, were as follows:

- $J_t(x) \approx \pm$ 5000 pA.m^{-2} for $t = 2$ ms (fig. 21a);
- $J_n(x) \approx \pm$ 14000 pA.m^{-2} for $t = 4$ ms (fig. 21b);
- $J_d(x) \approx \pm$ 14000 pA.m^{-2} for $t = 5$ ms (fig. 22a);
- $J_{n,d}(x) \approx \pm$ 16.5 pA.m^{-2} for $t = 100$ ms (fig. 22b).

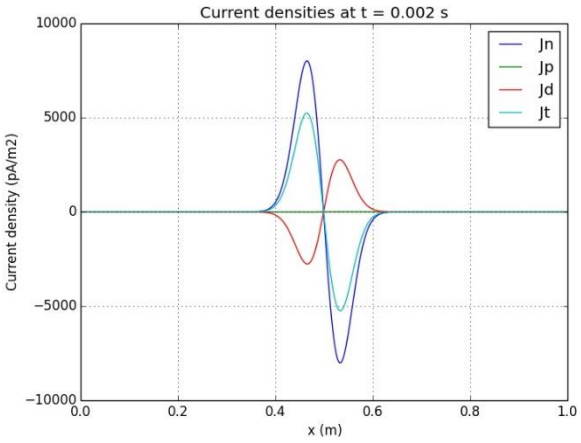

Fig. 21a: Current densities plot for $Vapp = 0.0$ V and $t = 2$ ms.

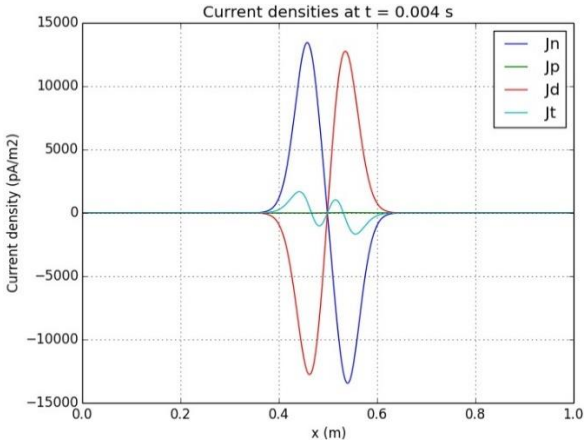

Fig. 21b: Current densities plot for $Vapp = 0.0$ V and $t = 4$ ms.

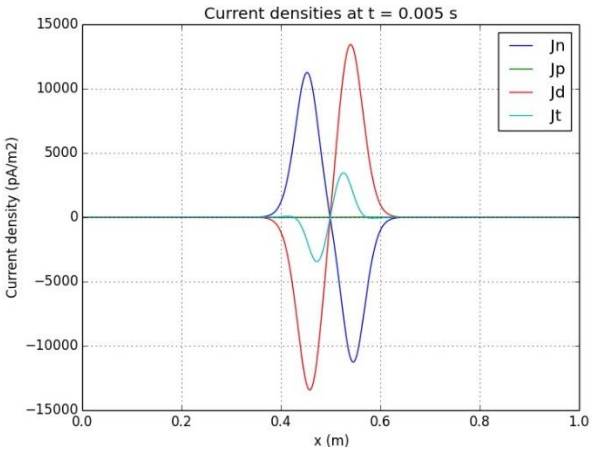

Fig. 22a: Current densities plot for $Vapp = 0.0$ V and $t = 5$ ms.

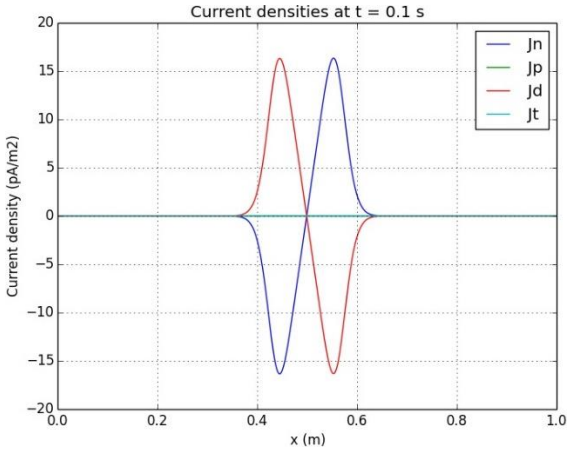

Fig. 22b: Current densities plot for $Vapp = 0.0$ V and $t = 100$ ms.

The current density of positive ions exhibits much lower values when compared to the other components of the current densities. $J_t(x)$ reaches the highest value for $t = 2$ ms and after that event it decreases. However, the other two components of total current density, $J_n(x)$ and $J_d(x)$, behave differently. After reaching the initial maximum peak ($t = 5$ ms), they decrease in value and it is possible to observe current reversing polarity at $t \approx 60$ ms (fig. 23). It is possible to see a new increase in value until they reach a local maximum (~16.5 pA.m^{-2}) at $t \approx 100$ ms (fig. 22b). Then $J_n(x)$ and $J_d(x)$ fade away on approach to equilibrium state.

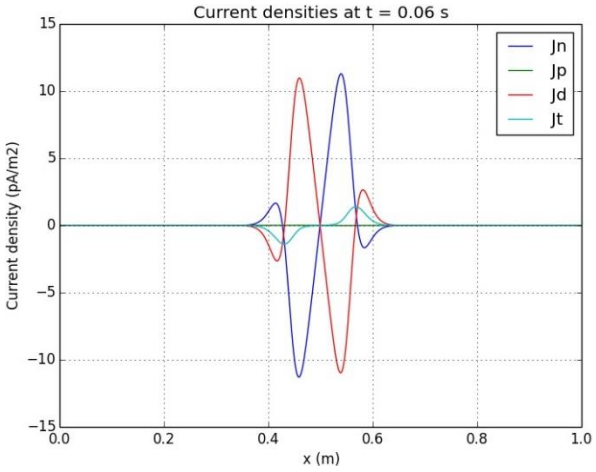

Fig. 23: Current densities plot for $Vapp = 0.0$ V and $t = 60$ ms.

In fig. 24, it is represented the current versus potential applied curve which shows that the current increases almost linearly with the increase of V_{app}, as was also seen in fig. 14. The increase can be considered linear for $V_{app} \geq 3.0$ V and it is defined by $I = 1.12 \times 10^{-10} V_{app} + 1.00 \times 10^{-11}$ (A) (red line), with a degree of correlation equal to 0.99997. However, for $V_{app} < 3.0$ V, it is possible to see a small curvature, which was not present in the last section. We can also see in this case, that for higher values of Vapp, the behavior of *I(Vapp)* does not change.

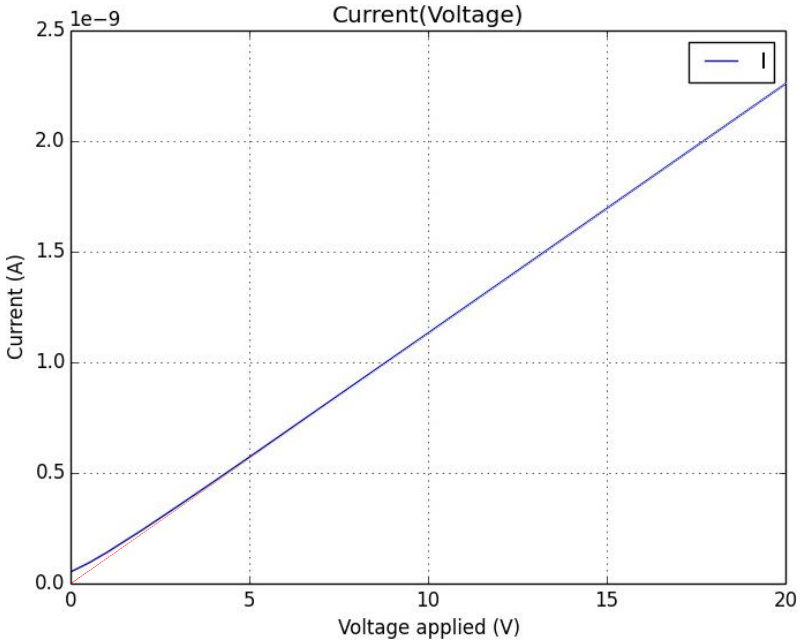

Fig. 24: $I(Vapp)$ plot for $Vapp = [0.0\,, 20.0]$ V.

4.1.3. Exponential time decay and Gaussian in the deformation region (G_c)

We can observe, in fig. 25, the variation of potential, for $V_{app} = 0.0$ V, registering a peak of ~ 43 mV at $t \approx 60$ ms, due to the generation rate function G_c , shown in fig. 26 and defined as:

- $A = 10^{15}\ m^{-3}s^{-1}$
- $\tau = 1$ ms
- $x_c \approx 25$ cm
- $\sigma_x \approx 2.4$ cm

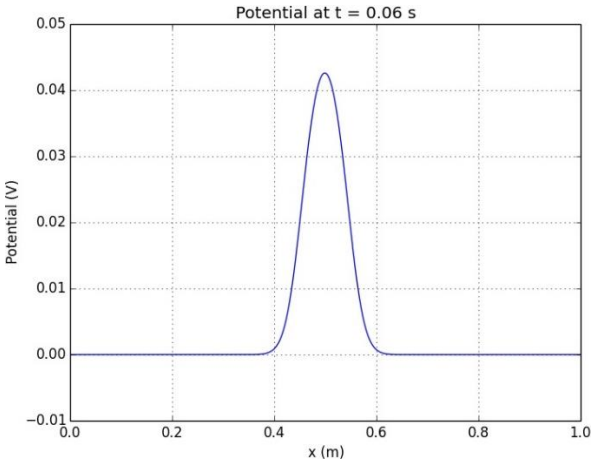

Fig. 25: V(x) plot with applied potential of 0.0 V for $t = 60$ ms.

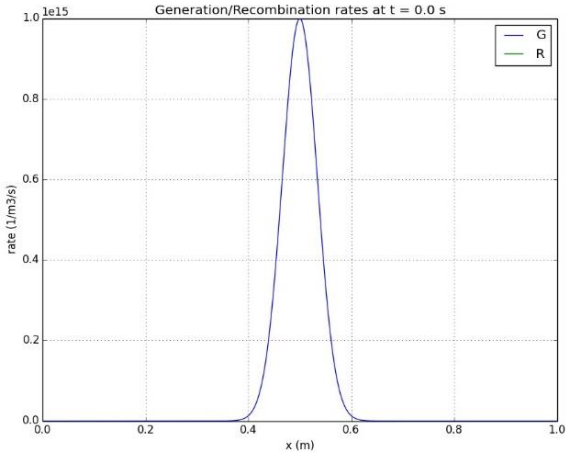

Fig. 26: G(x) and $R(x)$ plot for $Vapp = 0.0$ V and $t = 0.0$ s.

The electric field registered the maximum values for t = 60 ms, with applied voltage equal to 0.0 V and 20.0 V (fig. 27a and fig. 27b).

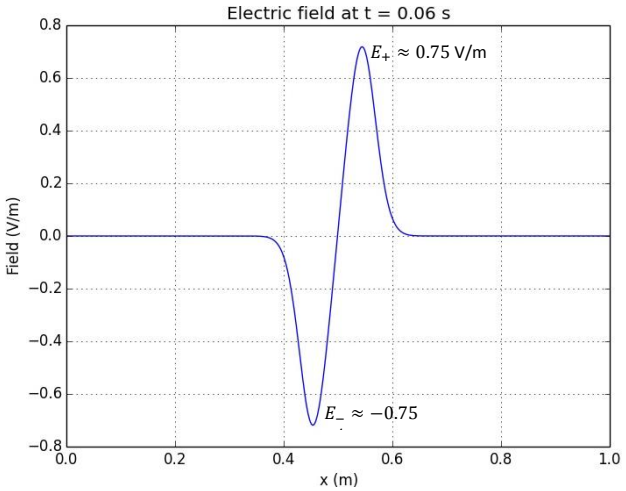

Fig. 27a: $E(x)$ plot for $Vapp = 0.0$ V and $t = 60$ ms.

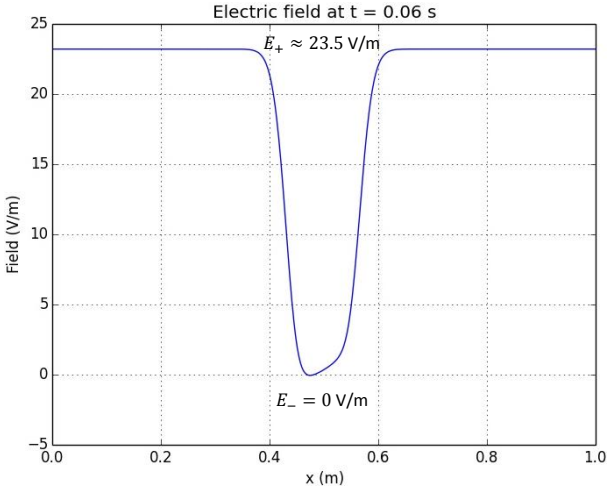

Fig. 27b: $E(x)$ plot for $Vapp = 20.0$ V and $t = 60$ ms.

The generation rate evolution is characterized by a decrease from its maximum value ($G_c = 10^{15}\ m^{-3}s^{-1}$) obtained at t = 0.0 s (fig. 26) and after that, a decrease until it reaches the zero value at $t \approx$

10 ms. The recombination rate gets to its maximum peak ($\sim 1.3 \times 10^{14}\ m^{-3}s^{-1}$) at t = 3 ms (fig. 28a) and then it decreases.

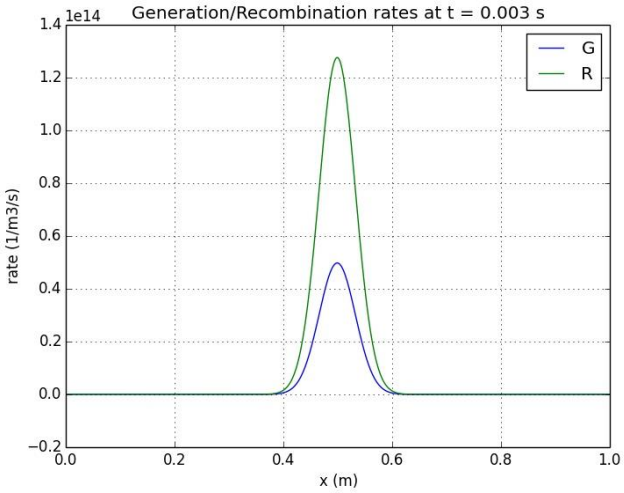

Fig. 28a: Plot maximum value of recombination rate for $Vapp = 0.0$ V.

In fig. 28b it is represented the plot which describes the recombination rate evolution, for $V_{app} = 0.0$V. The type of curves presented in the two graphs above are equal to the plot of fig.18b and fig. 18c, respectively, with the exception of presenting a smaller variation of the recombination rate. The value of recombination rate also increases with V_{app}, as we can see in fig. 28c, presenting a value higher than in fig. 28b. Looking to the above graphs, we can see that the values of $R(x)$ registered reached a smaller peak than in the previous two subchapters.

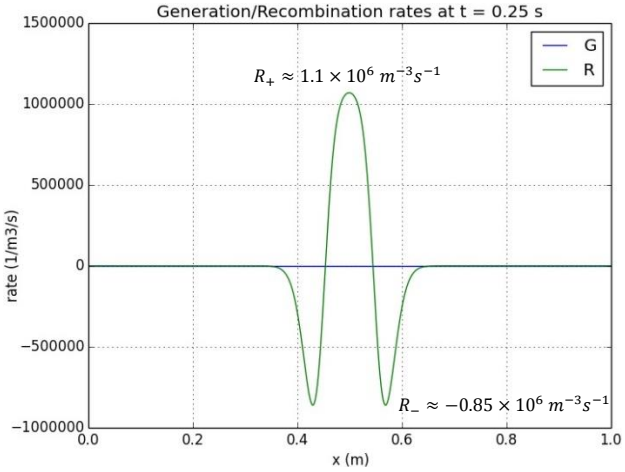

Fig. 28b: Plot of recombination rate evolution with $Vapp = 0.0$ V.

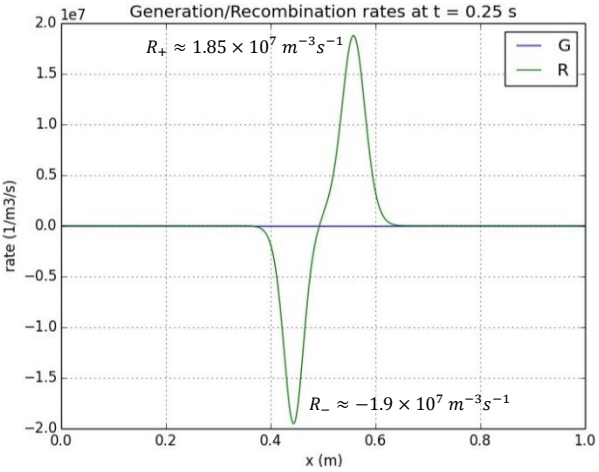

Fig. 28c: Plot of R(x) evolution with $Vapp = 20.0$ V.

The maximum values of $n(x)$ and $p(x)$ were obtained for $t = 3$ ms (fig. 29a), and the highest value of $\rho(x)$ was registered for $t \approx 40$ ms (fig. 29b).

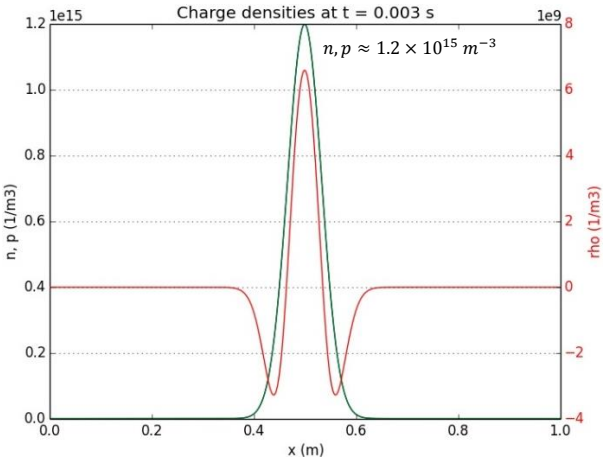

Fig. 29a: $n(x)$, $p(x)$ and $\rho(x)$ plot for $Vapp = 0.0$ V and $t = 3$ ms.

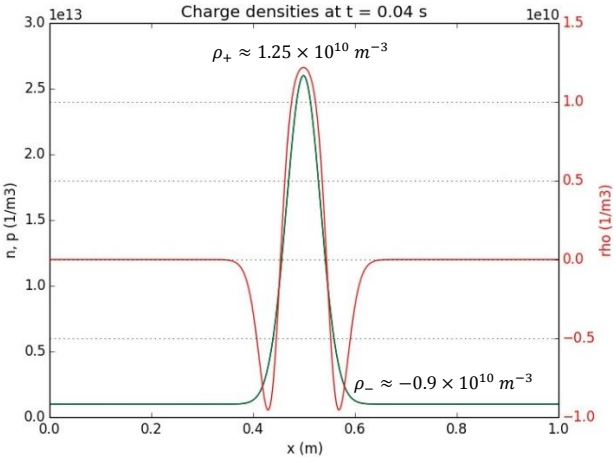

Fig. 29b: $n(x)$, $p(x)$ and $\rho(x)$ plot for $Vapp = 0.0$ V and $t = 40$ ms.

It is possible to verify some variations between $t \approx 100$ ms and $t \approx 130$ ms. The equilibrium form of $n(x)$ and $p(x)$ is represented below (fig. 30a and 30b).

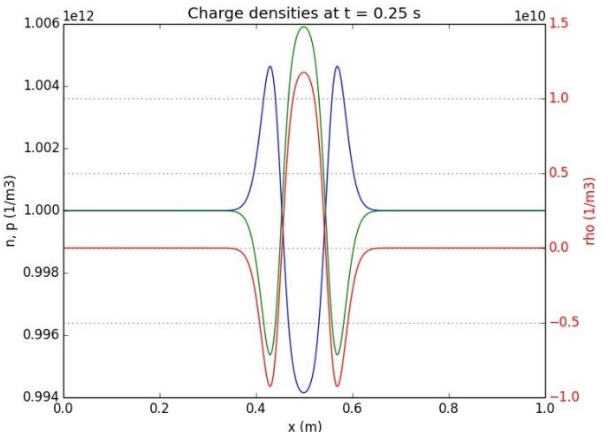

Fig. 30a: $n(x)$, $p(x)$ and $\rho(x)$ plot for $Vapp = 0.0$ V.

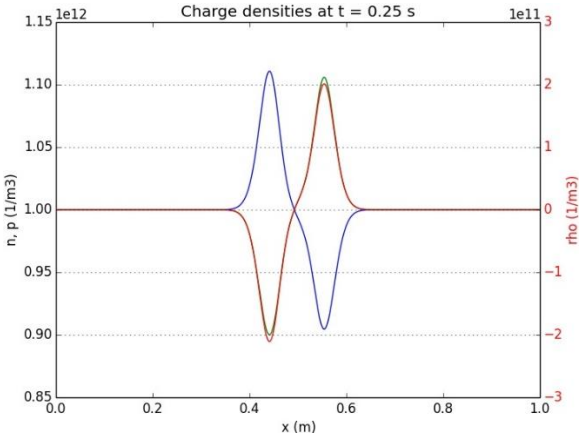

Fig. 30b: $n(x)$, $p(x)$ and $\rho(x)$ plot for $Vapp = 20.0$ V.

The graphs shown in fig. 30a and fig. 30b, presents a curve with the same characteristics as seen in fig. 20a and fig. 20b. Looking at fig. 30a, we can note a smaller maximum variation of $n(x)$ and $p(x)$ (~ 0.6 %). From fig. 30b we can see that the variation of this parameters also increase with the increase of V_{app}, as we have seen before, and the maximum variation of the concentration of electrons and positive ions is ~11 % for $V_{app} = 20.0$ V.

The maximum values of current densities obtained for $V_{app} = 0.0$ V, were as follows:

- $J_t(x) \approx \pm$ 2800 pA.m^{-2} for $t = 1$ ms (fig. 31a);
- $J_n(x) \approx \pm$ 8500 pA.m^{-2} for $t = 2$ ms (fig. 31b);
- $J_d(x) \approx \pm$ 8500 pA.m^{-2} for $t = 3$ ms (fig. 32a);
- $J_{n,\mathrm{d}}(x) \approx \pm$ 11.5 pA.m^{-2} for $t = 110$ ms (fig. 32b).

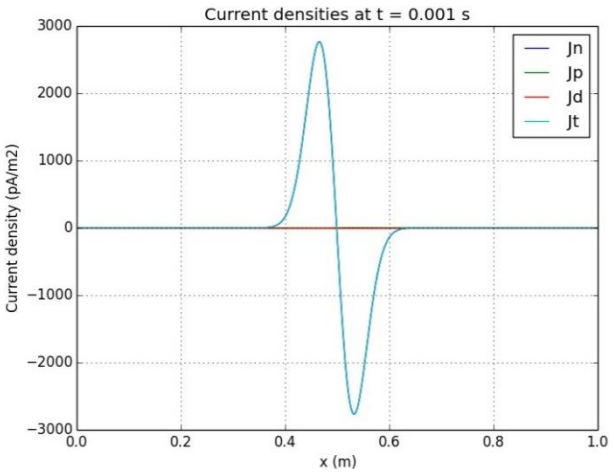

Fig. 31a: Current densities plot for $Vapp = 0.0$ V and $t = 1$ ms.

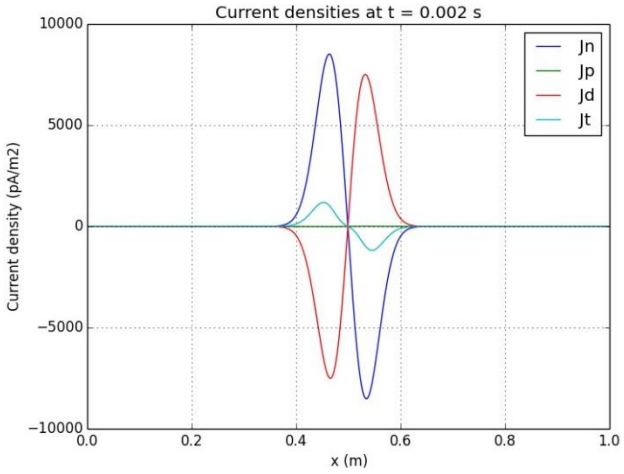

Fig. 31b: Current densities plot for $Vapp = 0.0$ V and $t = 2$ ms.

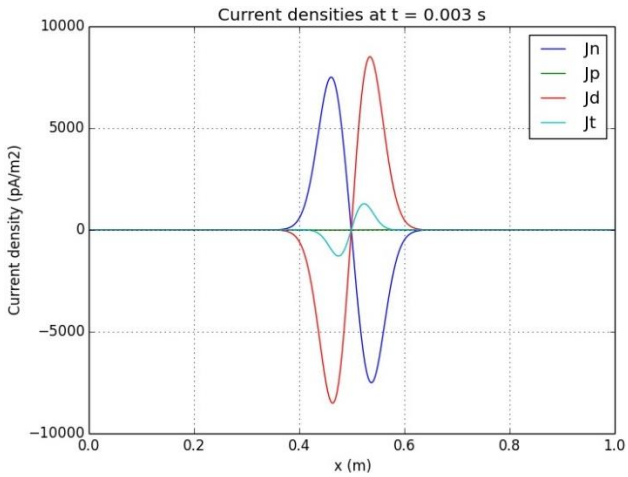

Fig. 32a: Current densities plot for $Vapp = 0.0$ V and $t = 3$ ms.

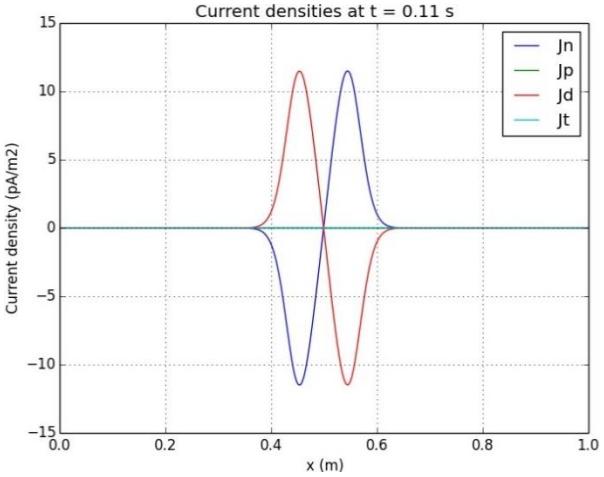

Fig. 32b: Current densities plot for $Vapp = 0.0$ V and $t = 110$ ms.

The current density of positive ions exhibits much lower values when compared to the other components of the current densities. $J_t(x)$ reaches the highest value for $t = 1$ ms and after that event it decreases. $J_n(x)$ and $J_d(x)$, have the same behavior as the previous function. After reaching the initial maximum peak ($t = 3$ ms), they decrease in value and it is possible to observe current reversing polarity at $t \approx 60$ ms (fig. 33). We can see a new increase in value until they reach a local maximum at $t \approx 110$ ms (fig. 32b). Then $J_n(x)$ and $J_d(x)$ fade away on approach to equilibrium state.

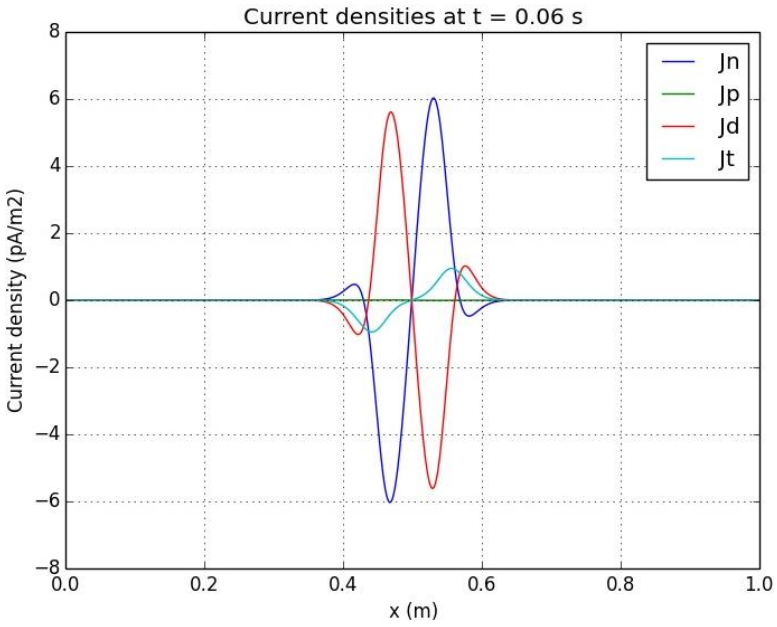

Fig. 33: Current densities plot for $Vapp = 0.0$ V and $t = 60$ ms.

In fig. 34, it is represented the current versus potential applied curve, and its behavior is almost equal to the curve presented in fig. 24, presenting a small curvature for $V_{app} < 3.0$ V as seen in the last sub-chapter. The increase can be considered linear for $V_{app} \geq 3.0$ V and it can be defined by the function $I = 1.58 \times 10^{-10} V_{app} + 2.00 \times 10^{-11}$ (A) (red line), with a degree of correlation equal to 0.99994.

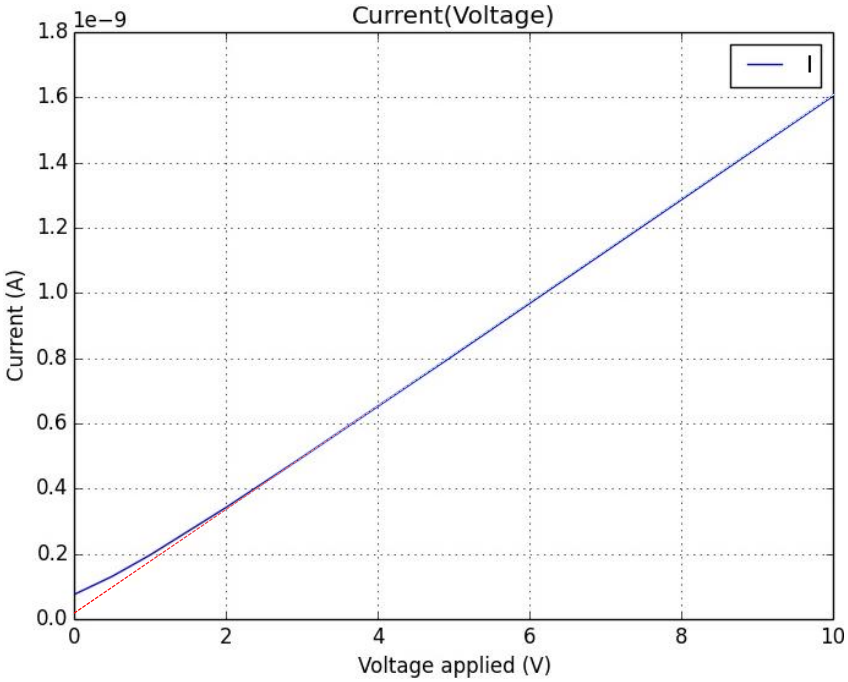

Fig. 34: $I(Vapp)$ plot.

4.1.4. Gaussian time pulse and Gaussian centered in the borders of the deformation region (G_d)

It can be seen from fig. 35, the variation of potential, for $V_{app} = 0.0$ V, reaching two peaks of 63 mV at *t* = 50 ms, due to the Generation rate function G_d (fig. 36) defined as:

- $A = 10^{15}\ m^{-3}s^{-1}$
- $t_c = 2$ ms
- $\sigma_x \approx 2.4$ cm
- $\sigma_t = 1$ ms

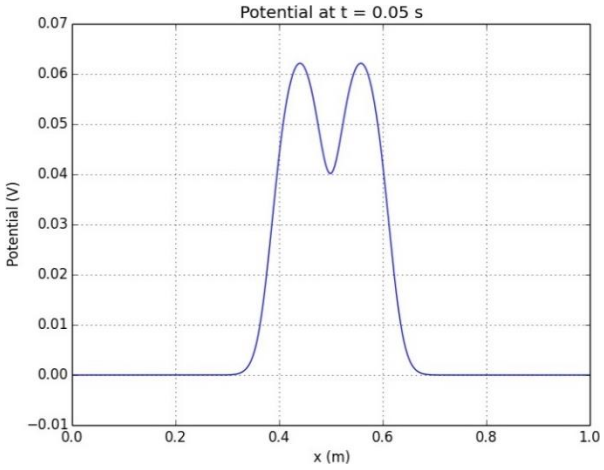

Fig. 35: $V(x)$ plot for $V_{app} = 0.0$ V.

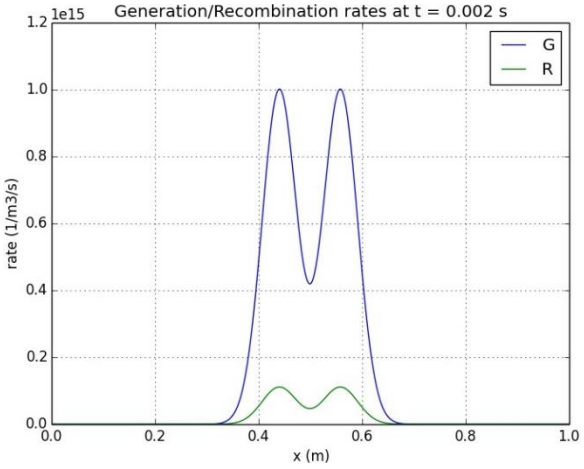

Fig. 36: $G_d(x)$ plot for $t = 2$ ms.

The electric field registered the maximum values for *t* = 60 ms, with applied voltage equal to 0.0 V and 20.0 V (fig. 37a and fig. 37b).

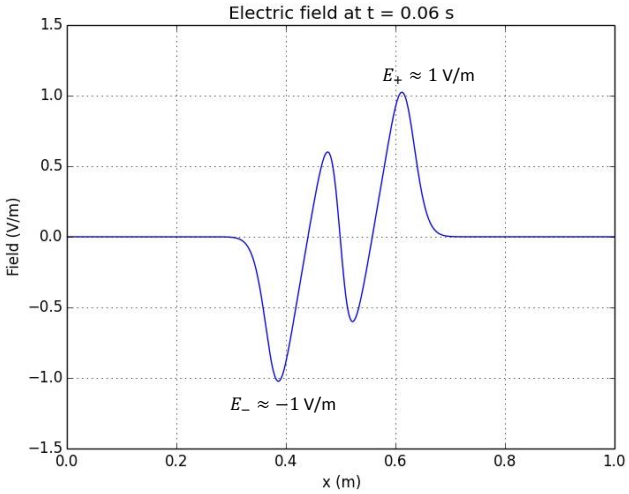

Fig. 37a: $E(x)$ plot for $Vapp = 0.0$ V and $t = 60$ ms.

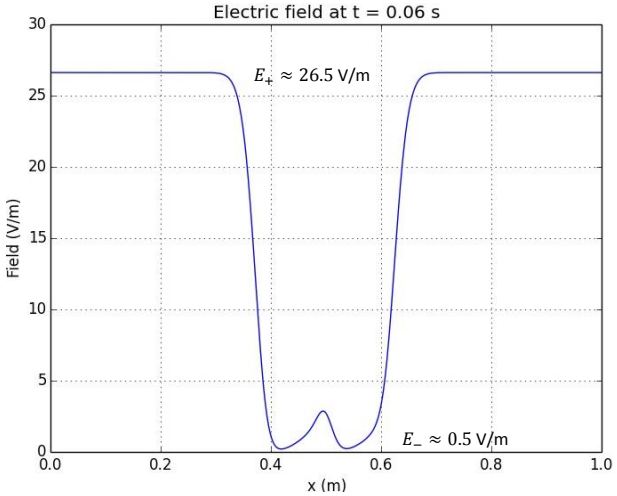

Fig. 37b: $E(x)$ plot for $Vapp = 20.0$ V and $t = 60$ ms.

The generation rate plot over time, show us an increase of its value until at *t* = 2 ms (fig. 36) it reaches its maximum value ($G_d = 10^{15}\ m^{-3}s^{-1}$). After that point it vanishes after *t* ~ 15 ms. The behavior of

the recombination rate is similar, when compared to the last two sections and the point where it meets its maximum ($\sim 2.7 \times 10^{14}\ m^{-3}s^{-1}$) is at t = 5 ms (fig. 38a).

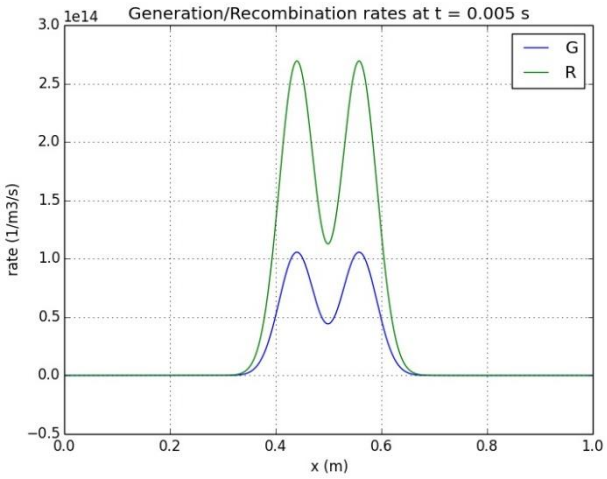

Fig. 38a: Plot with maximum value of Recombination rate for V_{app} = 0.0 V.

The graphs below show us a more complex variation of the recombination rate, due to the behavior of the generation rate function, when compared to the previous subsections of Chapter 4. Comparing fig. 38c with fig. 38b, it is possible to observe the increase of recombination with the rise of V_{app}.

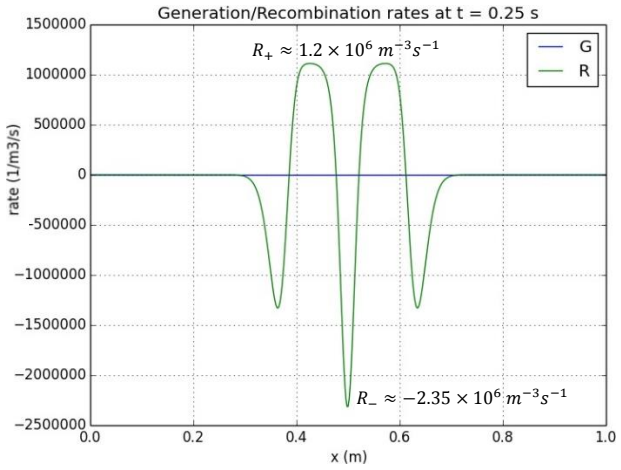

Fig. 38b: Plot of Recombination rate evolution with V_{app} = 0.0 V.

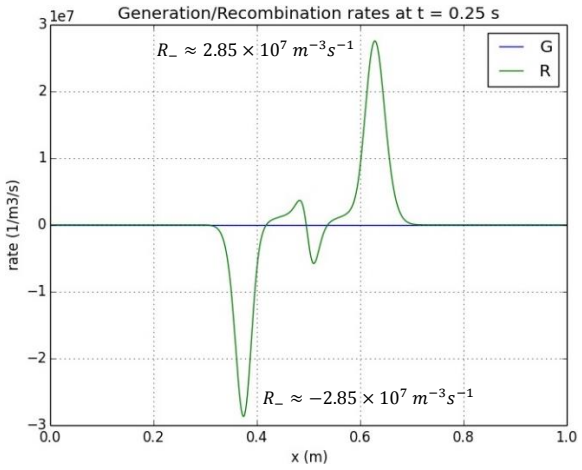

Fig. 38c: Plot of R(x) evolution with V_{app} = 20.0 V.

The maximum values of $n(x)$ and $p(x)$ were obtained for t = 4 ms (fig. 39a), and the highest value of $\rho(x)$ was registered for $t \approx$ 40 ms (fig. 39b).

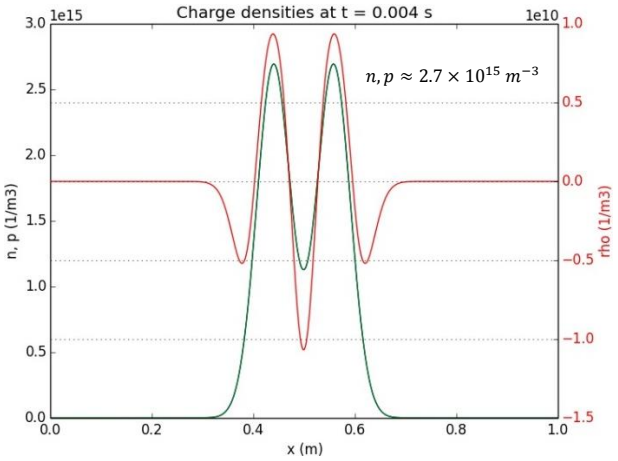

Fig. 39a: $n(x)$, $p(x)$ and $\rho(x)$ plot for $Vapp = 0.0$ V and $t = 4$ ms.

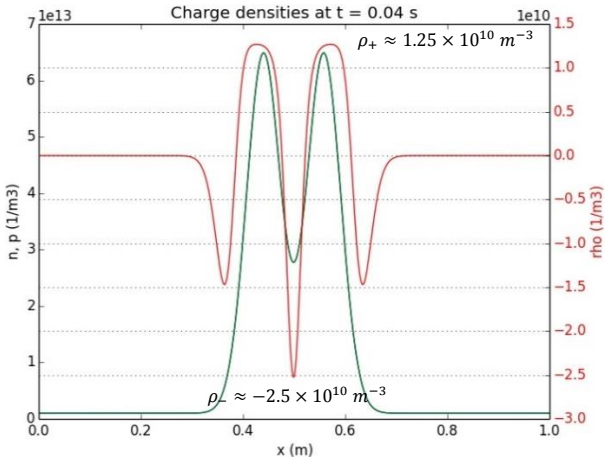

Fig. 39b: $n(x)$, $p(x)$ and $\rho(x)$ plot for $Vapp =$ and $t = 40$ ms.

It is possible to verify some variations between $t \approx 100$ ms and $t \approx 140$ ms. The stable form of $n(x)$ and $p(x)$ is represented below (fig. 40a and 40b).

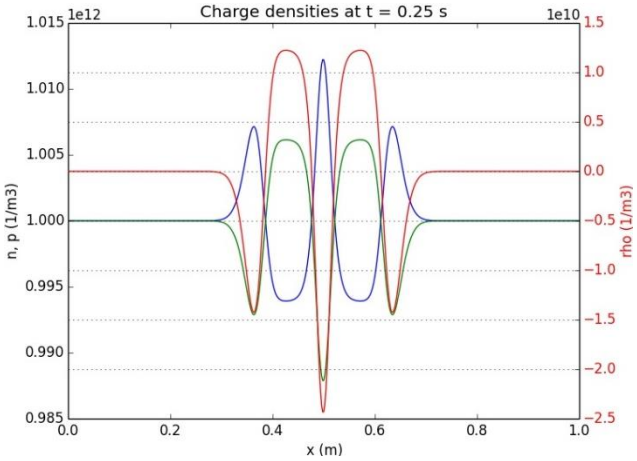

Fig. 40a: $n(x)$, $p(x)$ and $\rho(x)$ plot for $Vapp = 0.0$ V.

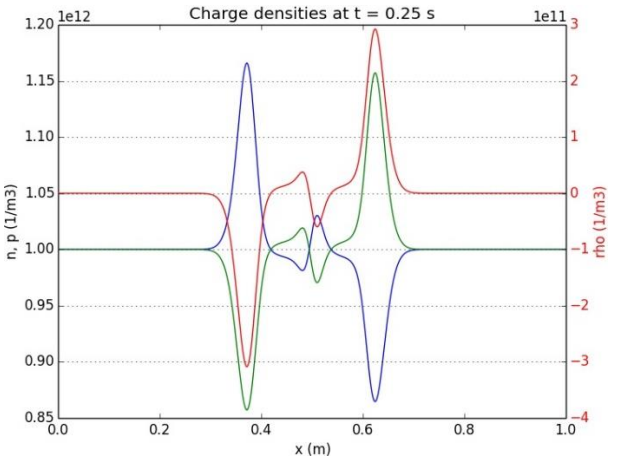

Fig. 40b: $n(x)$, $p(x)$ and $\rho(x)$ plot for $Vapp = 20.0$ V.

The concentration of electrons and positive ions, due to the behavior of the generation rate function, presents a more complex behavior, such as the recombination rate analysis stated before. Aside from that factor, the oscillation of $n(x)$, $p(x)$ and $\rho(x)$ also increased from the plot in fig. 40a to the plot in fig. 40b, as seen before. For $V_{app} = 0.0$ V, $R(x)$ oscillates a maximum of 1.25 % and in fig. 40b, we can see that the maximum variation is around 17 %.

The maximum values of current densities obtained were as follows:

- $J_t(x) \approx \pm$ 5000 pA.m^{-2} for $t = 2$ ms (fig. 41a);
- $J_n(x) \approx \pm$ 14000 pA.m^{-2} for $t = 4$ ms (fig.41b);
- $J_d(x) \approx \pm$ 14000 pA.m^{-2} for $t = 5$ ms (fig. 42a);
- $J_{n,d}(x) \approx \pm$ 16.5 pA.m^{-2} for $t = 110$ ms (fig. 42b).

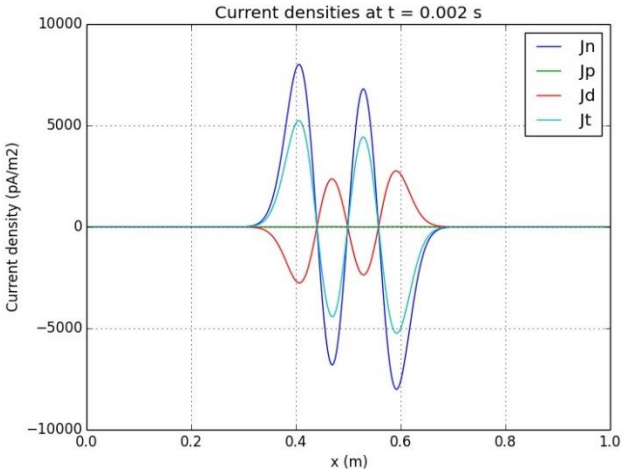

Fig. 41a: Current densities plot for $Vapp = 0.0$ V and $t = 2$ ms.

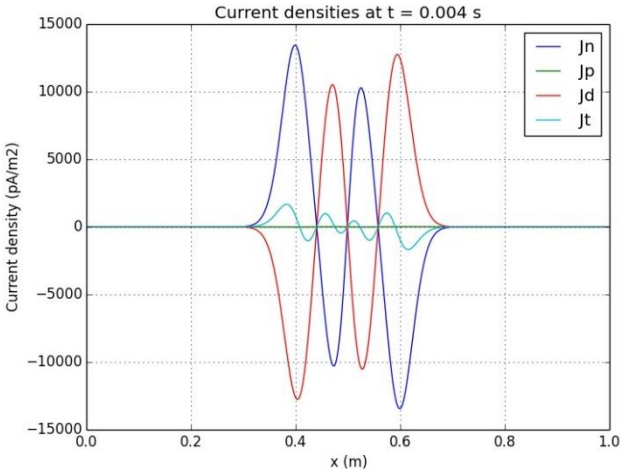

Fig. 41b: Current densities plot for $Vapp = 0.0$ V and $t = 4$ ms.

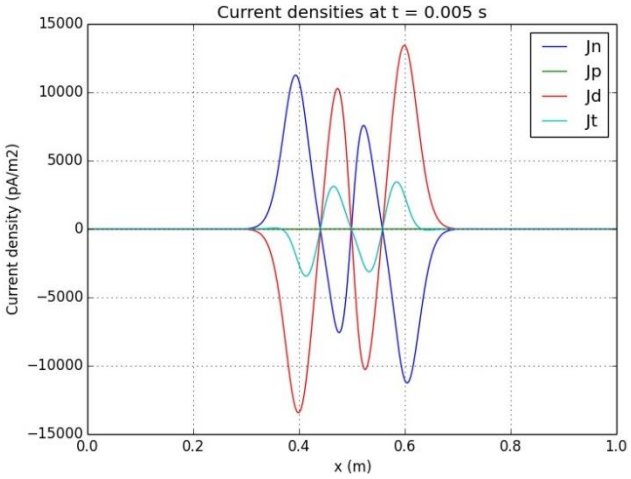

Fig. 42a: Current densities plot for $Vapp = 0.0$ V and $t = 5$ ms.

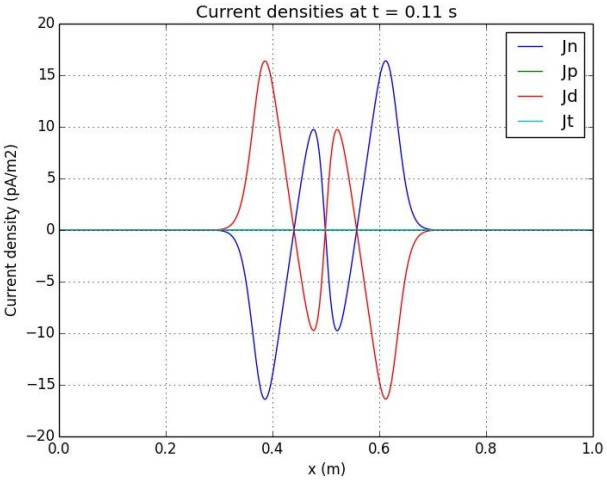

Fig. 42b: Current densities plot for $Vapp = 0.0$ V and $t = 110$ ms.

The current density of positive ions exhibits much lower values when compared to the other components of the current densities. $J_t(x)$ reaches the highest value for $t = 2$ ms and after that event it decreases. The values of $J_n(x)$ and $J_d(x)$ decrease, after they reach the initial maximum peak at t = 5 ms and it is possible to observe current reversing polarity at $t \approx 60$ ms (fig. 43). We can see a new increase in value till they reach a local maximum at $t \approx 110$ ms (fig. 42b). Then, the values of $J_n(x)$ and $J_d(x)$ decrease on approach to equilibrium state.

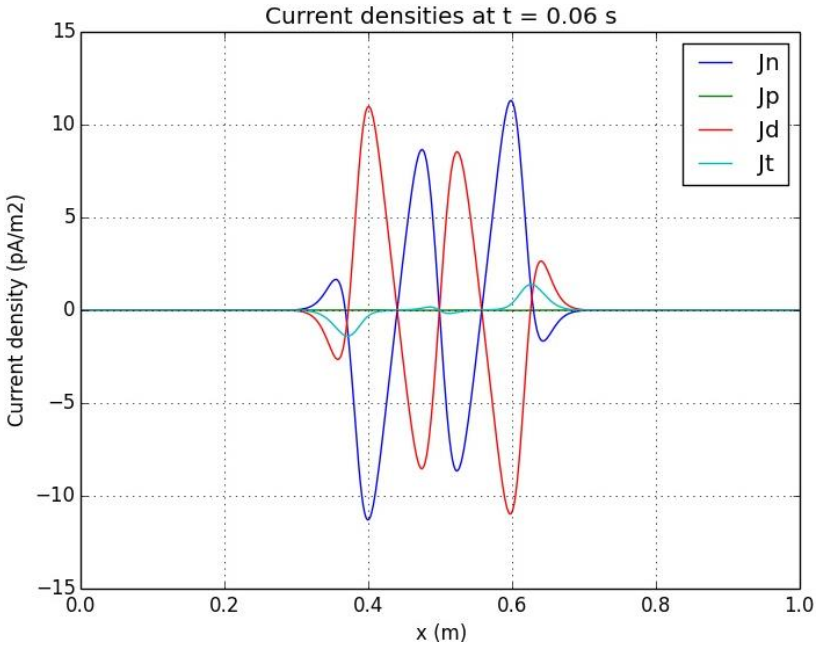

Fig. 43: Current densities plot for $Vapp = 0.0$ V and $t = 60$ ms.

From fig. 44, we can see the same type of graph as the previous two subchapters. The obtained curve is almost linear for values of $V_{app} \geq 3.0$ V and it can be approximated as $I = 1.18 \times 10^{-10} V_{app} + 1 \times 10^{-11}$ (A) (red line), with a degree of correlation equal to 0.99994.

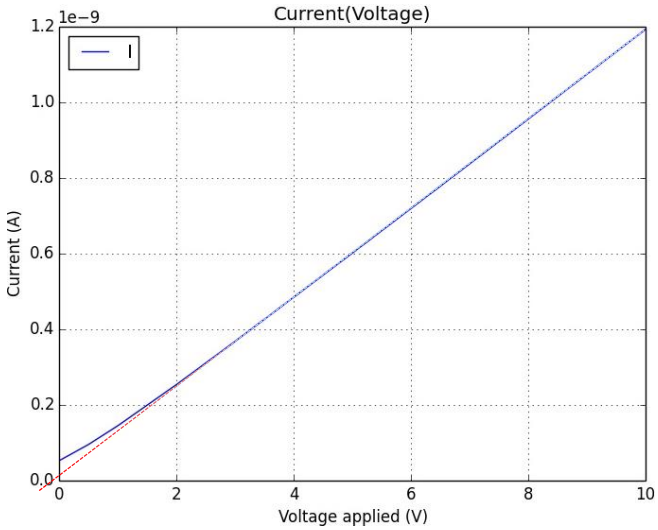

Fig. 44: $I(Vapp)$ plot.

4.1.5. Exponential time decay and Gaussian centered in the borders of the deformation region (G_e)

It is represented in fig. 45, the variation of V(x), for V_{app} = 0.0 V and t = 60 ms, reaching two maximum values of potential ($V \approx$ 43 mV), due to the generation rate function G_e (fig. 46) defined as:

- $A = 10^{15}\ m^{-3}s^{-1}$
- τ = 1 ms
- $\sigma_x \approx$ 2.4 cm

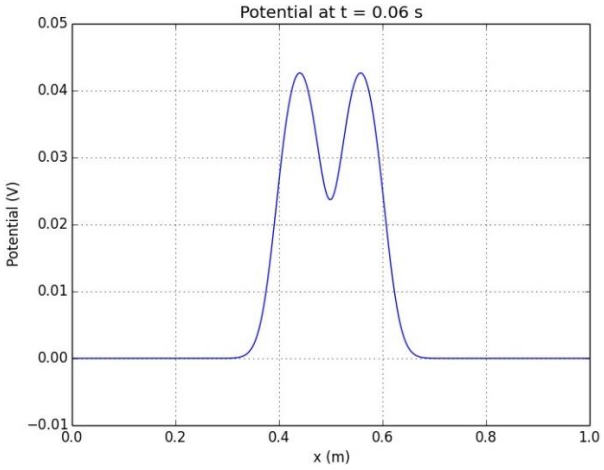

Fig. 45: $V(x)$ plot for $Vapp$ = 0.0 V and t = 60 ms

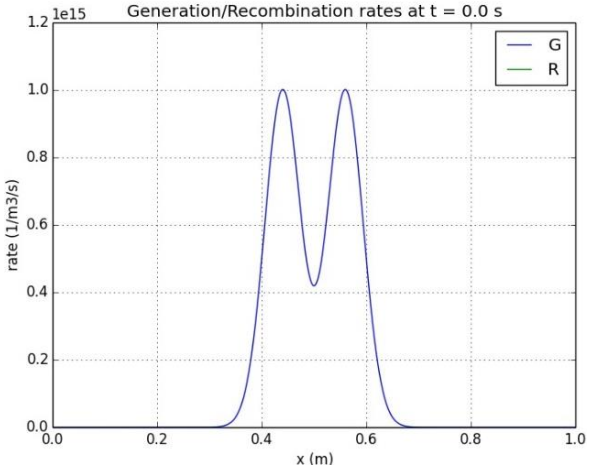

Fig. 46: $G_e(x)$ plot for t = 0.0 s.

The electric field registered the maximum values for t = 60 ms, with applied voltage equal to 0.0 V and 20.0 V (fig. 47a and fig. 47b).

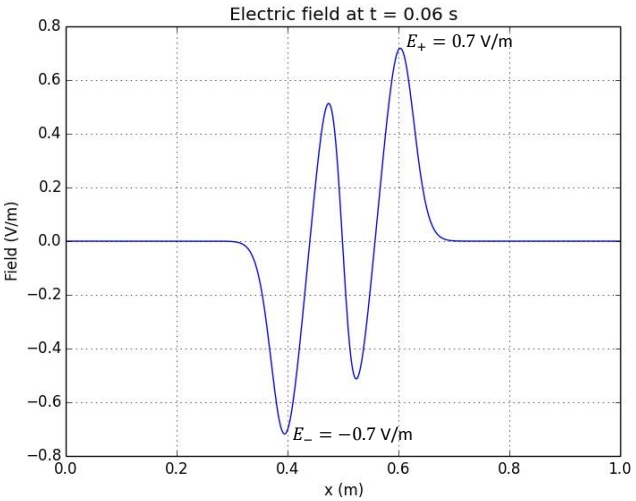

Fig. 47a: $E(x)$ plot for $Vapp$ = 0.0 V and t = 60 ms.

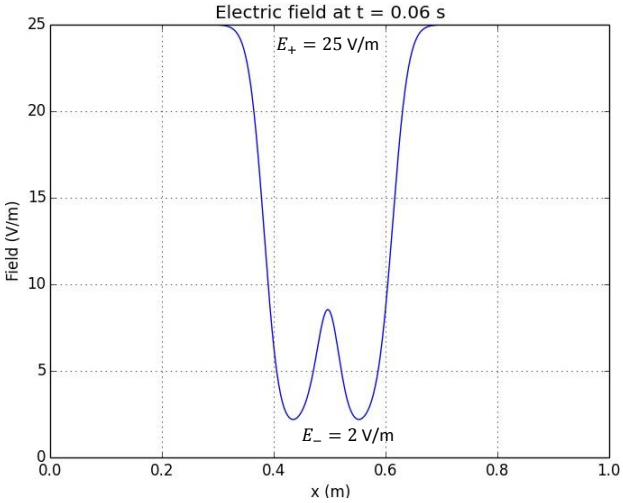

Fig. 47b: $E(x)$ plot for $Vapp$ = 20.0 V and t = 60 ms.

Although the generation rate presents a curve similar to function G_d, it reaches its maximum value for *t* = 0.0 s (fig. 46) and vanishes at *t* ≈ 30 ms. The recombination rate presents the maximum peak ($\sim 1.3 \times 10^{14}\ m^{-3}s^{-1}$) for *t* = 0 ms (fig. 48a).

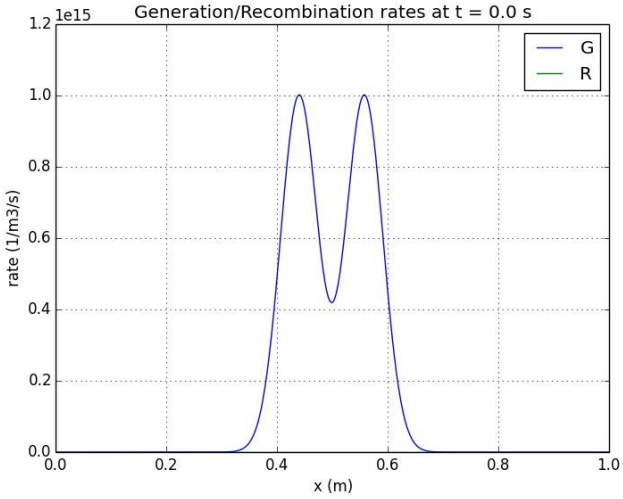

Fig. 48a: Plot with the maximum value of recombination rate for $Vapp = 0.0$ V.

In fig. 48b and fig. 48c, we can see that the type of curve of recombination rate is very similar to the previous subchapter, with the difference of presenting lower values of R(x) for *t* = 250 ms.

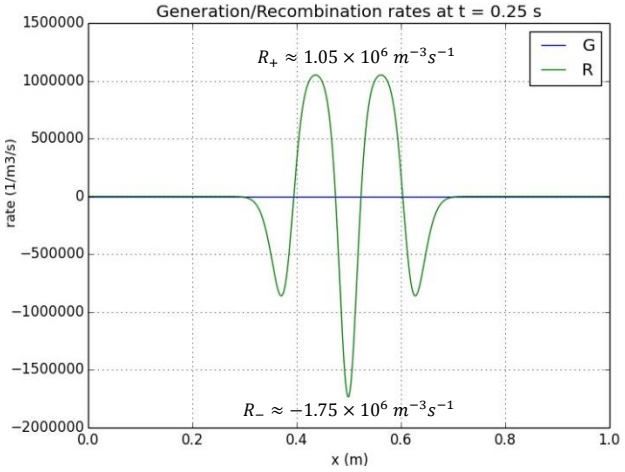

Fig. 48b: Plot of recombination rate evolution with $Vapp = 0.0$ V.

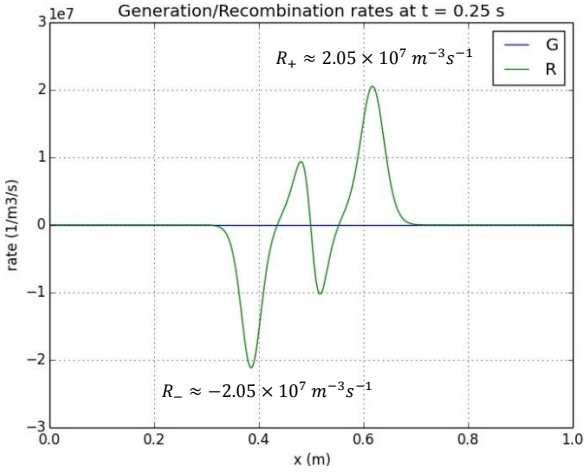

Fig. 48c: Plot of R(x) evolution with $Vapp = 20.0$ V.

The maximum values of $n(x)$ and $p(x)$ were obtained for $t = 2$ ms (fig. 49a), and the highest value of $\rho(x)$ was registered for $t \approx 40$ ms (fig. 49b).

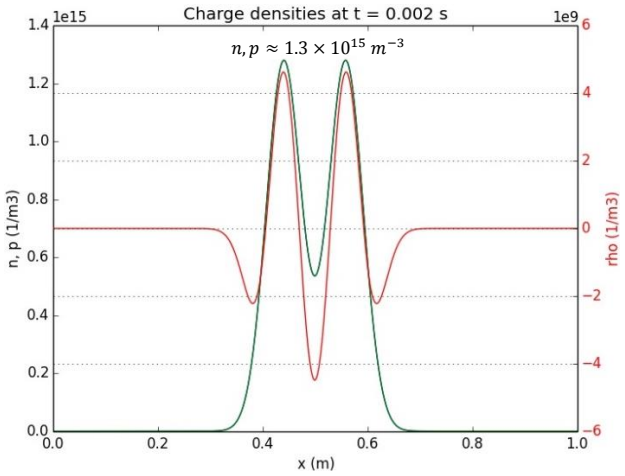

Fig. 49a: $n(x)$, $p(x)$ and $\rho(x)$ plot for $Vapp = 0.0$ V and $t = 2$ ms.

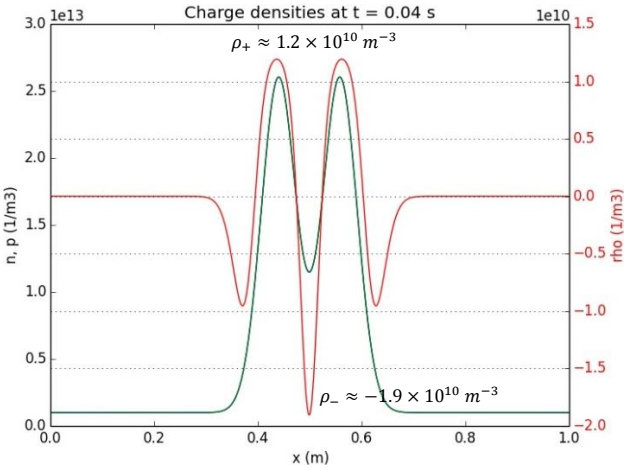

Fig. 49b: $n(x)$, $p(x)$ and $\rho(x)$ plot for $Vapp = 0.0$ V and $t = 40$ ms.

It is possible to verify some variations between $t \approx 100$ ms and $t \approx 140$ ms. The equilibrium form of $n(x)$ and $p(x)$ is represented below.

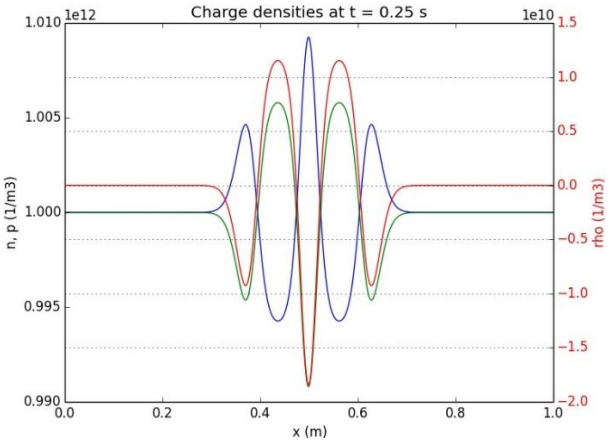

Fig. 50a: $n(x)$, $p(x)$ and $\rho(x)$ plot for $Vapp = 0.0$ V.

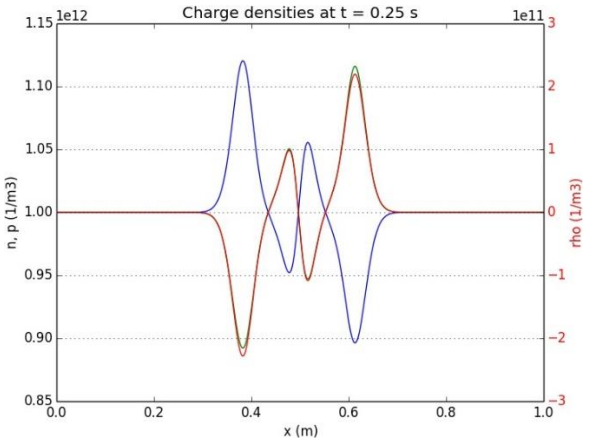

Fig. 50b: $n(x)$, $p(x)$ and $\rho(x)$ plot for $Vapp = 20.0$ V.

Once again, just as the previous analysis, the concentration of electrons and positive ions represented in fig. 50a and fig 50b, are similar to the data from fig. 40a and fig. 40b. The maximum oscillation of $n(x)$ and $p(x)$ in this case is ~ 0.9 % and 12 %.

The maximum values of current densities obtained were as follows:

- $J_t(x) \approx \pm$ 7800 pA.m^{-2} for $t = 1$ ms (fig. 51a);
- $J_n(x) \approx \pm$ 8000 pA.m^{-2} for $t = 2$ ms (fig. 51b);
- $J_d(x) \approx \pm$ 8000 pA.m^{-2} for $t = 3$ ms (fig. 52a);
- $J_{n,d}(x) \approx \pm$ 16.5 pA.m^{-2} for $t = 110$ ms (fig. 52b).

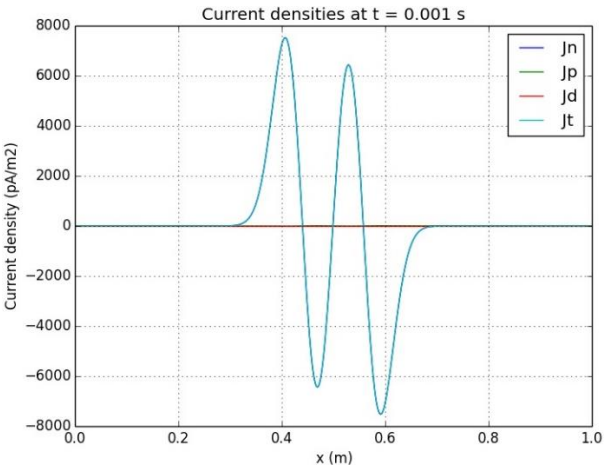

Fig. 51a: Current densities plot for $Vapp = 0.0$ V and $t = 1$ ms.

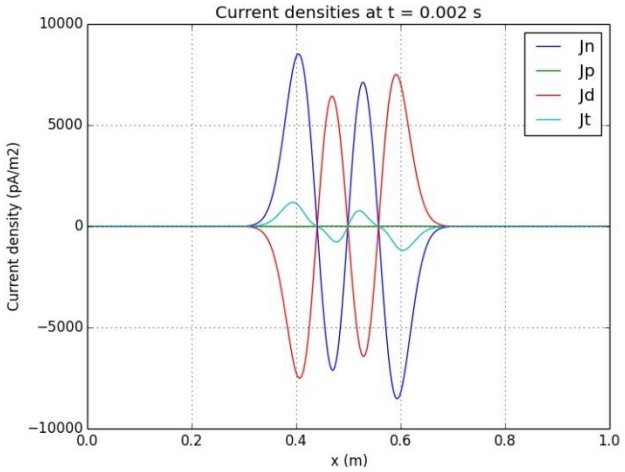

Fig. 51b: Current densities plot for $Vapp = 0.0$ V and $t = 2$ ms.

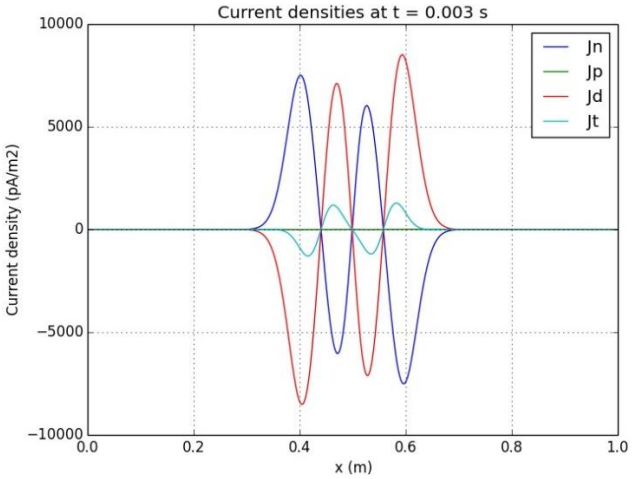

Fig. 52a: Current densities plot for $Vapp = 0.0$ V and $t = 3$ ms.

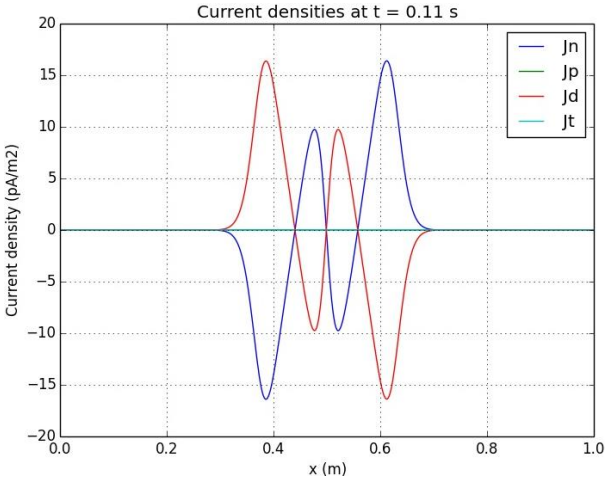

Fig. 52b: Current densities plot for $Vapp = 0.0$ V and $t = 110$ ms.

The current density of positive ions exhibits much lower values when compared to the other components of the current densities. $J_t(x)$ reaches the highest value for $t = 1$ ms and after that event it decreases. $J_n(x)$ and $J_d(x)$, present the same behavior of the last sections. After they reach the initial maximum peak ($t = 3$ ms), occurs a decrease in value and it is possible to observe current reversing polarity at $t \approx 60$ ms (fig. 53). We can see a new increase in value till they reach a local maximum at $t \approx 110$ ms (fig. 52b). Then $J_n(x)$ and $J_d(x)$ decrease to values close to zero, on approach to equilibrium state.

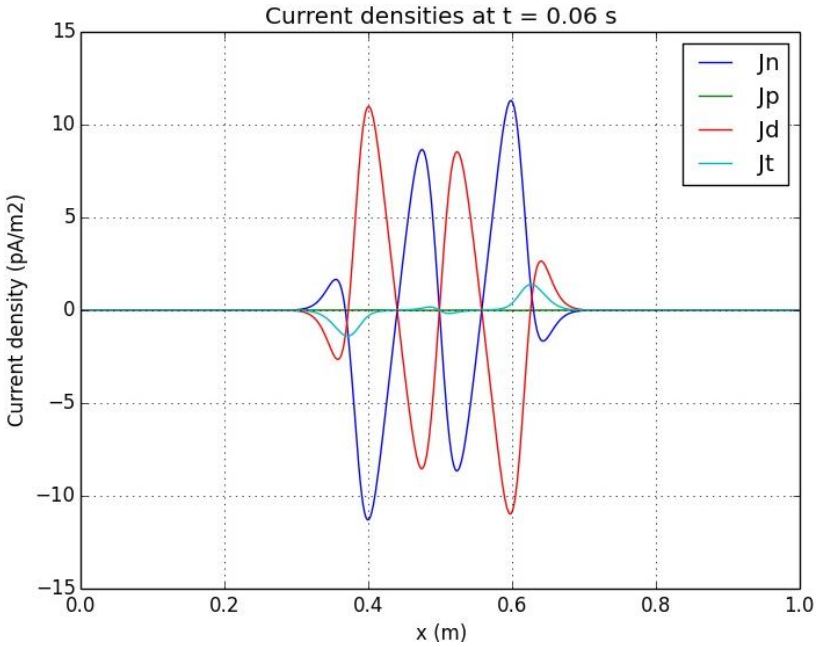

Fig. 53: Current densities plot for $Vapp = 0.0$ V and $t = 60$ ms.

From fig. 54, we can see the same type of graph as the previous three subchapters. The function that approximates the $I(V_{app})$ graph, for values of $V_{app} \geq 3.0$ V is represented by $I = 1.58 \times 10^{-10} V_{app} + 1 \times 10^{-11}$ (A) (red line), with a linear correlation factor equal to 0.99997. It is very similar to the values obtained in fig. 34, reaching 1.61×10^{-9} A for $V_{app} = 10$ V.

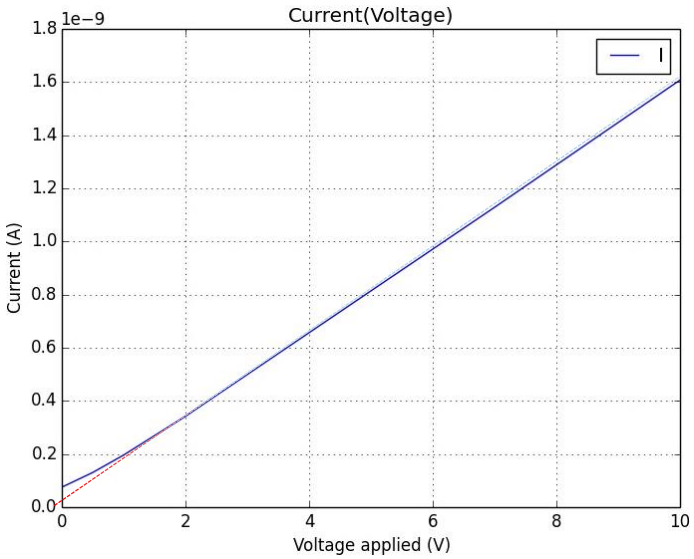

Fig. 54: $I(Vapp)$ plot.

4.2. Variable applied potential

With the implemented code, there is also the possibility of setting the applied potential variable in time (eq. 25). We defined the parameters as $A_V = 5.0$ V and $w = 50\,\pi\, rad.s^{-1}$ ($\tau = \frac{1}{50\pi} \sim 6.4$ ms $\gg \Delta t$. The results above mentioned were simulated with G_e as the generation rate function, defined in section 4.1.5.

In fig. 55a, we have the current evolution during 0.5 s of simulation time. It is possible to see that the maximum current is obtained in the beginning of the experience, for *t* = 2 ms (fig. 55b). After the transient effect, the oscillation of current follows the potential oscillation with an amplitude that is an increasing function of A_V. If we used a cosine function instead, the value of current for $t = 0.0$ s would be nonzero.

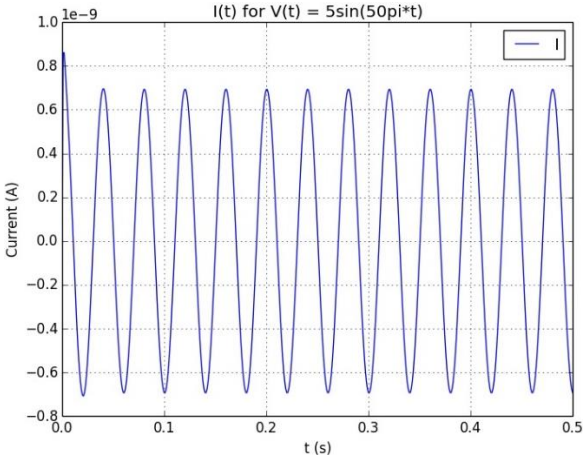

Fig. 55a: $I(t)$ plot for $V(t) = 5\,\sin(50\pi t)$.

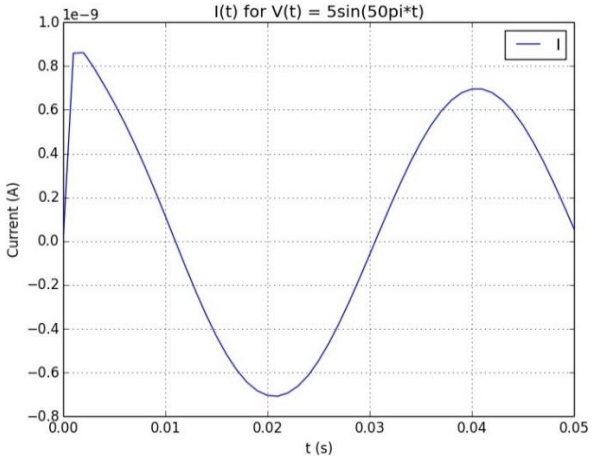

Fig. 55b: $I(t)$ zoomed plot for $V(t) = 5\,\sin(50\pi t)$.

We can see in fig. 56 the variation of current with *V(t)*. It is possible to confirm that the maximum value of current is obtained at the beginning of the simulation (*t* = 2 ms). The maximum mismatch between current oscillation and potential oscillation is $\sim 1.83 \times 10^{-10}$ A which corresponds to a maximum oscillation of ~27%. After ~17 ms of simulation time, the values of current approach the equilibrium behavior.

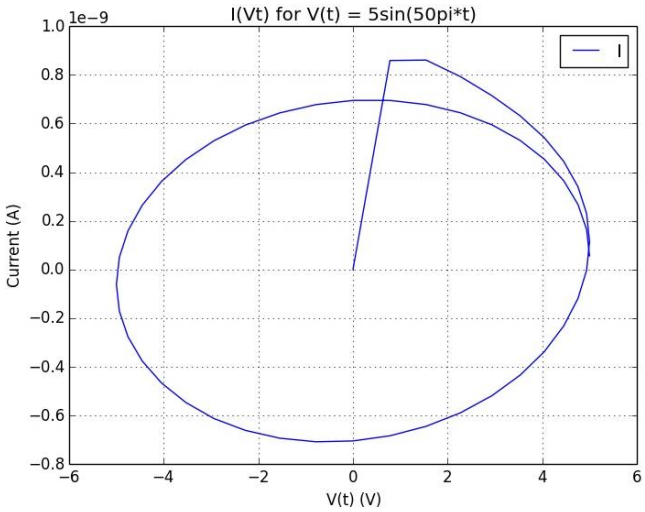

Fig. 56: $I(Vt)$ for $V(t) = 5\,\sin(50\pi t)$.

We have made also simulations for different values of applied potential bias, $V_0 \in [0,\ 50]$ V, with fixed values of $A_V = 5$ V and w $= 50\,\pi\ rad.s^{-1}$. The results for the $I(V_0)$ curve are shown in fig. 57a. It is possible to observe similarities when compared to the $I(V)$ plots from the previous subchapter 4.1. We verified a linear increase with slope 1.59×10^{-10} A.V^{-1} and a linear correlation factor equal to 1.0.

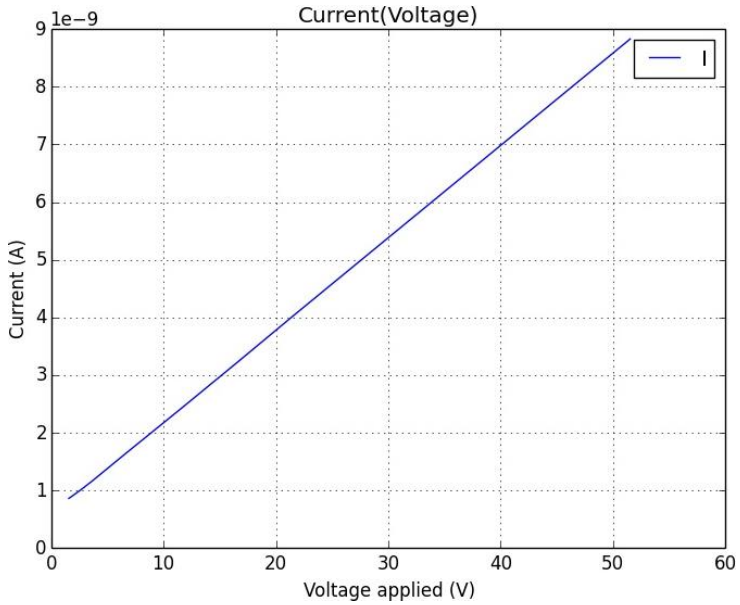

Fig. 57a: $I(V_0)$ for $V(t) = V_0 + 5\,\sin(50\pi t)$.

From fig. 57b, we can see the I(A_V) curve for different values of amplitude, $A_V \in [0, 10]$ V, with fixed values of $V_0 = 0$ V and w $= 50\,\pi\ rad.s^{-1}$. In fig. 57c, it is represented the I(w) plot which consider a variable value of angular frequency, w$\in [0, 100\pi]\ rad.s^{-1}$ with fixed values of $V_0 = 0$ V and $A_V = 5$ V. We also verified a linear increase for the first case with slope 1.61×10^{-10} A.V^{-1} and a degree of correlation equal to 1.0.

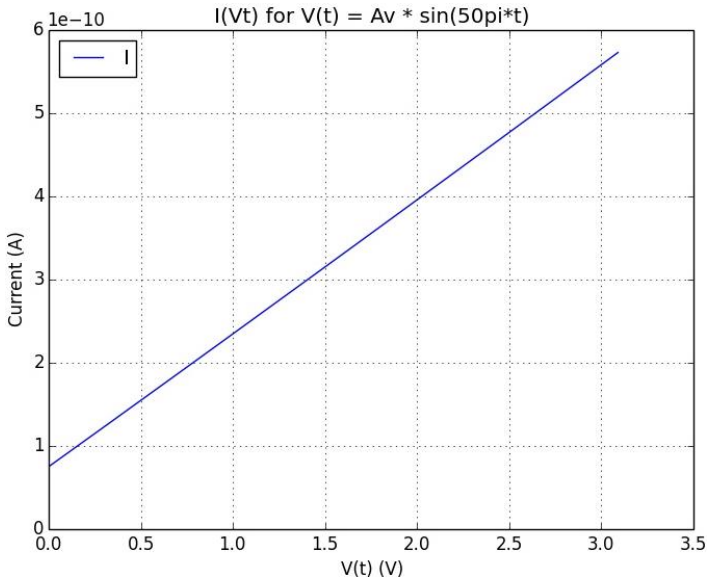

Fig. 57b: $I(V_0)$ for $V(t) = A_V \sin(50\pi t)$.

The simulation performed with variable w presented a small curvature (fig. 57c), however, for values of w≥ 70π, we registered a slope of 5.77×10^{-10} A.V^{-1} (red line) and linear correlation factor equal to 0.99997.

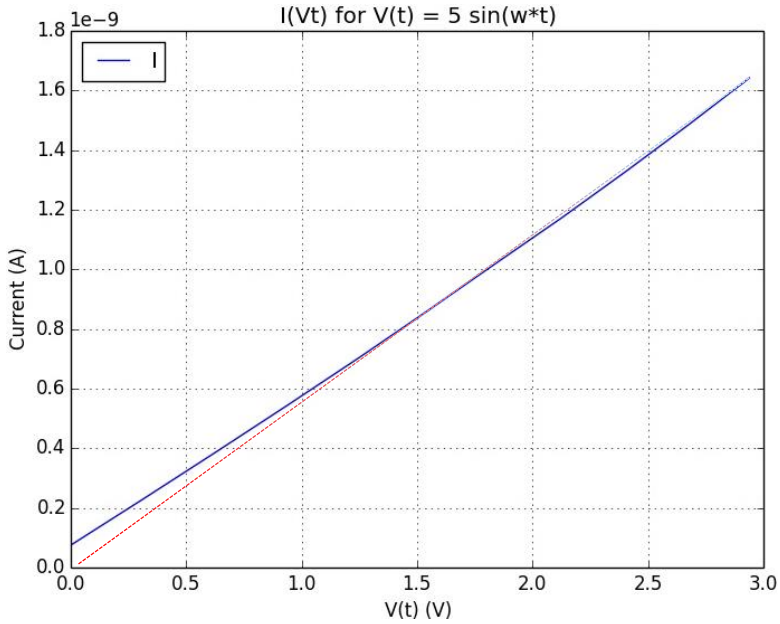

Fig. 57c: $I(V_0)$ for $V(t) = 5 \sin(wt)$.

Chapter 5

Discussion

Considering the fact that the n-p recombination time was equal to 5.0 s, we set a simulation time of $t_{exp} = 0.25$ s. However we realized that almost all the changes happened in the first moments of the simulation. The duration of the charge generation events is much shorter than the n-p recombination time. After the charge generation event occurs, there is only recombination until the total charge density vanishes in all the lattice nodes.

The maximum value of current, occurs for a time of the order of the event duration. So the calculation of $I(V_{app})$ was possible to be simulated with a much higher value of iterations (10 000), and in a shorter time range, without spending too much simulation time. In section 4.1.1, we choose a higher value of iterations (1000 iterations) and a larger time of experience ($t_{exp} = 1.0$ s), in order to better observe the graphs.

From sections 4.1.2 to 4.1.5, it is possible to see that the maximum values of potential and electric field occur for the same time, and the maximum values of n(x), p(x), $J_n(x)$ and $J_d(x)$, also occur for the same time. In section 4.1.1, the maximum value of potential was reached for $t \sim 60$ ms and the maximum values of electric field were obtained for $t \sim 40$ ms.

Considering all the simulations performed, we could see that the total current density and the generation rate registered the same behavior. They both reached maximum values in the beginning of the simulation and then decreased their value approaching to zero, presenting the generation rate a faster convergence to that value. The concentrations of positive ions and electrons started with maximum values in the beginning of the simulation (t ~ 5ms) and then decreased its value. It is possible to verify that between $t \sim 100$ ms and $t \sim 150$ ms occur some changes in both curves. The ion current density presents the lowest values of the 3 components of total current density, as expected and the values of $J_n(x)$ and $J_d(x)$, after reaching a peak in the initial moments of the simulation, it is possible to see a decrease in both values and for $t \sim 60$ ms (currents reverse polarity) a new increase is observed, which can be related with the time when the maximum values of potential were obtained. A local maximum is registered for both components for $t \sim 100$ ms and finally they decrease, fading away to equilibrium state. $J_n(x)$ and $J_d(x)$ presented the same behavior in all simulations registering similar values.

The $I(V_{app})$ plots from sections 4.1.2 and 4.1.5 where all similar, showing a linear increase with a small curvature for lower values of Vapp, only presenting some differences in the values obtained, due to the effects of the respective generation rate functions. We can compare these results with the

experimental results obtained by F. T. Freund with a dry gabbro sample [27] (fig. 58). In section 4.1.1, the *I(V)* curve also increases linearly, except for the fact that for low values of Vapp, there is no curvature.

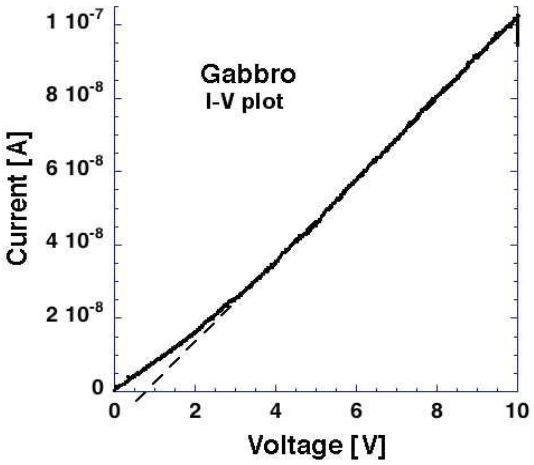

Fig. 58: Experimental $I(V)$ plot of a dry gabbro sample [27].

In section 4.1, it was verified the decrease of the values of recombination rate, and concentration of electrons and positive ions over time, in all cases, as expected from what was mentioned above. The values of V_{app}, were also directly related with the oscillation of values of $R(x), n(x)$ and $p(x)$. In sections 4.1.2 and 4.1.4 (G_b and G_d functions respectively), we registered the highest values for maximum variation of $R(x)$, $n(x)$ and $p(x)$, and in section 4.1.1 (G_a function) we obtained the lowest results.

In chapter 4.2, we observed the effects in current, due to variations of angular frequency, bias and amplitude. The bias influences the value of current registered, the amplitude is associated with oscillations of current and angular frequency is related with the number of cycles of current registered within the simulation time. We used equation 25 and we could infer that the type of $I(V)$ curve is equal to the other examples in chapter 4. The maximum values of current were obtained once again in the initial moments of the simulation. The use of a cosine function implies a nonzero value for $t = 0.0$ s.

All *I(V)* plots presented a ohmic behavior, except for lower values of applied potential in the cases where was a visible curvature. It can be compared to a *n-p-n* bipolar junction curve.

Chapter 6

Conclusions and further work

In this dissertation, it was presented a model capable of simulating numerically electrical transport in rocks under mechanical action. Some simulations were performed using five different types of generation functions capable of describing different phenomena and/or simulation regimes. We could infer that generation function G_a required more work in order to determine $R(x)$, $n(x)$ and $p(x)$, as well the $I(V)$ plot. It would require a smaller lattice spacing, in order to see with more detail the concentration of positive ions and electrons, and the recombination rate.

Some comparisons were initially performed with different values of iterations. When we set the value $\tau_{np} = 1.0\ s$ the differences were substantial. However with $\tau_{np} = 5.0\ s$, the differences can be considered negligible.

During the charge generation phase, we could see that a positive potential barrier and n-p-n bipolar junction is formed and grows in the deformation region. We could also see that currents reversed polarity.

During the charge recombination phase, electrical signals decrease on approach to electrical equilibrium.

The effects in current, due to variations of angular frequency, bias and amplitude were analyzed in section 4.2.

It was also possible to verify the validity of the results in comparison with an experimental *I(V)* curve obtained with a sample of a dry Gabbro.

As a future work, the simulations could be extended to two and three dimensions.

References

[1] Brace, W.F., 1975. Dilatancy-related electrical resistivity change in rocks. Pure Appl. Geophys. 113, 207–217.

[2] Brace, W.F., Paulding, B.W., Scholz, C., 1966. Dilatancy in the fracture of crystalline rocks. J. Geophys. Res. 71, 3939–3953.

[3] St-Laurent, F., 2000. The Saguenay, Québec, earthquake lights of November 1988–January 1989. Seismol. Res. Lett. 71, 160–174.

[4] Tsukuda, T., 1997. Sizes and some features of luminous sources associated with the 1995 Hyogo-ken Nanbu earthquake. J. Phys. Earth 45, 73–82.

[5] Liu, J. Y., Chen, Y. I., Chuo, Y. J., and Tsai, H. F.: Variations of ionospheric total electron content during the Chi-Chi earthquake, Geophy. Res. Lett., 28, 1383–1386, 2001.

[6] Pulinets, S. and Boyarchuk, K.: Ionospheric Precursors of Earthquakes, 350 pp., Springer Verlag, 2004.

[7] Ouzounov, D., Liu, D., Kang, C., et al.: Outgoing Long Wave Radiation Variability from IR Satellite Data Prior to Major Earthquakes, Tectonophysics, 431, 211–220, 2007.

[8] Tronin, A. A., Molchanov, O. A., and Biagi, P. F.: Thermal anomalies and well observations in Kamchatka, International Journal of Remote Sensing, 25, 2649–2655, 2004.

[9] Fujinawa, Y., Matsumoto, T., Iitaka, H., Takahashi, S. 2001. Characteristics of the Earthquake Related ELF/VLF Band Electromagnetic Field Changes, American Geophysical Union, Fall Meeting 2001. AGU, San Franscisco, CA, pp. #S42A-0616.

[10] Fujinawa, Y., Takahashi, K., 1990. Emission of electromagnetic radiation preceding the Ito seismic swarm of 1989. Nature 347, 376–378.

[11] Karakelian, D., Beroza, G. C., Klemperer, S. L., and Fraser-Smith, A. C.: Analysis of ultralow-frequency electrommagnetic field measurements associated with the 1999 M 7.1 Hector Mine, California, earthquake sequence, Bull. Seismol. Soc. Am., 92, 1513–2524, 2002.

[12] Loaiza, S., Fortin, J., Schubnel, a., Gueguen, Y., Vinciguerra, S., & Moreira, M. (2012). Mechanical behavior and localized failure modes in a porous basalt from the Azores. Geophysical Research Letters, 39(19). doi:10.1029/2012GL053218.

[13] Jouniaux, L., Zamora, M., & Reuschlé, T. (2006). Electrical conductivity evolution of non-saturated carbonate rocks during deformation up to failure. Geophysical Journal International, 167(2), 1017–1026. doi:10.1111/j.1365-246X.2006.03136.x

[14] Freund, F. T., Takeuchi, A., Lau, B. W. S., et al.: Stress-induced changes in the electrical conductivity of igneous rocks and the generation of ground currents, Terrestrial, Atmos. Oceanic Sci. (TAO), 15, 437-468, 2004.

[15] Freund, F. T.: On the electrical conductivity structure of the stable continental crust, J. Geodynamics, 35, 353–388, 2003.

[16] Freund, F.: Charge generation and propagation in rocks, J. Geodynamics, 33, 545–572, 2002.

[17] Selberherr, Siegfried (1984). Analysis and Simulation of Semiconductor Devices, Springer-Verlag, Wien-New York.

[18] Deinega, A., & John, S. (2012). Finite difference discretization of semiconductor drift-diffusion equations for nanowire solar cells. Computer Physics Communications, *183*(10), 2128–2135. doi:10.1016/j.cpc.2012.05.016.

[19] Vasileska, Dragica. Class Notes. Drift-Diffusion Model: Introduction, 9. Retrieved from https://nanohub.org/resources/1545/download/ddmodel_introductory_part_word.pdf, August 17, 2014.

[20] Ravaioli, Umberto. Class Notes: Review of Conventional Semiconductor Device Models based on partial differential equations, 1(2).

[21] Schenk, A. (1992). A model for the field and temperature dependence of Shockley-Read-Hall lifetimes in silicon, 1-12.

[22] Peir, J. (2005). Finite difference, Finite element and finite volume methods for partial differential, M, 1–32.

[23] Vasileska, Dragica. Class Notes. Numerical solution of Poisson's equation, 18. Retrieved from https://nanohub.org/resources/1542/download/numericalanalysis_ppt.pdf, August 17, 2014.

[24] Vasileska, Dragica. Class Notes. Drift-Diffusion Model: Time-Dependent Simulations Sharfetter-Gummel Discretization, 11. Retrieved from https://nanohub.org/resources/1575/download/ddmodel_sg_tds_word.pdf, August 17, 2014.

[25] Liu, J. (2011). Scharfetter-Gummel Method, 2011(September), 9–12.

[26] Frensley, W. R. (2004). Scharfetter-Gummel Discretization Scheme for Drift-Diffusion Equations, (3), 1–3.

[27] F. T. Freund. Pre-earthquake signals? Part I: Deviatoric stresses turn rocks into a source of electric currents. Natural Hazards and Earth System Science, 2007, 7 (5), pp.535-541.